Causal Analysis of Aerosol Impacts on Isolated Deep Convection: Findings from TRACER

Dié Wang[1], Roni Kobrosly[2], Tao Zhang[1], Tamanna Subba[1], Susan van den Heever[3], Siddhant Gupta[4], and Michael Jensen[1]

[1]Brookhaven National Laboratory, Upton, NY 11937
[2]Icahn School of Medicine at Mount Sinai, New York, NY 10029
[3]Colorado State University, Fort Collins, CO 80523
[4]Argonne National Laboratory, Lemont, IL 60439

Correspondence: Dié Wang (diewang@bnl.gov)

Abstract. This study employs a novel application of causal machine learning, specifically g-computation, to quantify aerosol effects on deep convective clouds (DCCs). Focusing on isolated DCCs in the Houston-Galveston region, we leverage comprehensive ground-based observations from the TRacking Aerosol Convection interactions ExpeRiment (TRACER) to estimate aerosol influences on convective core [c1]echo top height (ETH), intensity, and area. Our results show that greater aerosol number concentrations generally have a limited impact on these convective properties. Under optimal conditions, where ultrafine particles are effectively activated in updraft regions, aerosols exhibit a positive average causal effect on ETH, increasing it by approximately 1 km (13% of the average ETH). However, such conditions are difficult to achieve in the study region and have not been confirmed to occur. Additionally, it is inevitable to consider measurement uncertainties and the limitations of temporal and spatial resolution in the data, as these factors can further contribute to uncertainties in the estimates. In DCCs associated with sea breezes, aerosol effects are more pronounced, resulting in a 1.4 km deepening of ETH. However, this heightened effect could be attributed to the exclusion of key confounders such as boundary layer updrafts in the causal model. [c2]

1 Introduction

Deep convective clouds (DCCs) play a crucial role in the Earth's water cycle, as they generate a significant amount of global precipitation (e.g., Tan et al., 2015; Feng et al., 2016), regulate the global energy cycle through latent heat release (e.g., Tao et al., 2010), and vertical mass transport (e.g., Wang et al., 2019; Gupta et al., 2024), thereby driving large-scale atmospheric circulations that impact climate sensitivity (e.g., Sanderson et al., 2008; Del Genio, 2012). Despite their significance for weather

[c1] ~~depth, intensity, and area. Our results reveal that greater aerosol number concentrations generally have a limited impact on convective core echo top height (ETH), with an increase of about 1 km (13% of average ETH). This effect is observed under specific conditions, particularly when ultrafine particles are activated in updraft regions. Additionally, greater aerosol levels correspond to increased~~

and climate, accurately simulating DCCs in state-of-the-art numerical models remains challenging (e.g., Wang et al., 2020a; Prein et al., 2021; Wang et al., 2022b). Even fundamental convective characteristics such as updraft strength, cloud top height, and anvil mass detrainment, and the variations of these attributes over the diurnal cycle are difficult to simulate (e.g., Moncrieff, 2010; Bony et al., 2016). While field campaign data analyses have provided valuable insights into DCC processes (e.g., Polavarapu and Austin, 1979; Dye et al., 2000; Long et al., 2011; Chi et al., 2014; Barth et al., 2015; Jensen et al., 2016; Martin et al., 2017; Geerts et al., 2017; Varble et al., 2021; van den Heever et al., 2021; Jensen et al., 2022; Reid et al., 2023; Kollias et al., 2024), conventional model-observational validations mostly rely on bulk precipitation characteristics and/or sparse cloud dynamics observations from a small set of cases, thus offering only a limited understanding of the processes involved. Furthermore, case studies, by their nature, are confined to specific geographical regions, restricting model assessments to specific environmental forcing conditions (e.g., Prein et al., 2022; Ramos-Valle et al., 2023).

[c1] Aerosol-cloud interactions in DCCs are among the most complex and challenging processes to simulate accurately. This difficulty was evidenced in a recent model intercomparison project (MIP) conducted by the Deep Convective Working Groups of the Aerosols, Cloud, Precipitation and Convection (ACPC) initiative. This MIP was the first of its kind to assess the range of DCC sensitivity to aerosol loading across a suite of state-of-the-art convective system resolving models (van den Heever et al., 2018). Analysis of this suite of simulations conducted by Marinescu et al. (2021) focused on aerosol-induced changes to the terms in the vertical velocity momentum equation under prescribed low and high number concentrations of cloud condensation nuclei (CCN) conditions for a DCC case. This study showed substantial variability among the models in terms of the sensitivity of precipitation amount and updraft velocity to aerosol loading. The significant differences among the various models highlight an urgent need to resolve the lack of convergence in aerosol-DCC interaction process representations within such high-resolution modeling frameworks.

Numerous studies have aimed to shed light on the complex nature of aerosol-DCC interactions, towards improving their representations in the models, sparking the description of a number of different underlying physical mechanisms (e.g., Andreae et al., 2004; Khain et al., 2005; van den Heever et al., 2006; Rosenfeld et al., 2008; Lebo and Seinfeld, 2011; Li et al., 2011; Fan et al., 2018; Nishant et al., 2019; Grabowski and Morrison, 2020; Abbott and Cronin, 2021). The leading mechanisms include: (1) "cold-phase" invigoration, where high aerosol number concentrations, acting as CCN, nucleate more cloud droplets delaying hydrometeor growth via reduced collision-coalescence, lofting more liquid water above the freezing level, enhancing the total latent heating associated with freezing, increasing the buoyancy of rising convective parcels and ultimately invigorating convective updrafts (e.g., Khain et al., 2005; van den Heever et al., 2006; Rosenfeld et al., 2008); (2) "warm-phase" invigoration, where high aerosol number concentrations nucleate more cloud droplets and reduce supersaturation with respect to liquid water, increasing latent heat release through additional condensation of water vapor, and invigorating convective updrafts (e.g., Lebo, 2018; Fan et al., 2018, 2020); and (3) "humidity-entrainment" invigoration, where high aerosol number concentrations increase the environmental humidity by producing clouds that detrain more condensed water into the surrounding air, leading to higher humidity that favors large-scale ascent and stronger convective updrafts (Abbott and Cronin, 2021). This wide range of plausible mechanisms highlights the challenge of constraining this important problem with current observations. The lack of clear understanding further underscores the need for more robust and high-resolution observational data along with the

[c1] ~~Effective radiative forcing due to aerosol-cloud interactions stands out as the primary source of uncertainty associated with anthropogenic impacts on the climate system, according to the Intergovernmental Panel on Climate Change Sixth Assessment Report (IPCC, 2023). The challenging nature of accurately simulating aerosol-cloud interactions for DCCs~~

development of advanced statistical methods and modeling frameworks that can better elucidate the complexity of aerosol-DCC interactions.

Despite a range of hypothetical mechanisms for aerosol-DCC invigoration, recent studies continue to challenge [c1]these theories, revealing a spectrum ranging from enervation to invigoration (e.g., Grabowski and Morrison, 2020; Igel and van den Heever, 2021; Dagan, 2022; Romps et al., 2023; Peters et al., 2023). From an observational perspective, this challenge arises, in part, from a lack of key supporting observations of vertical velocity, hydrometeor microphysical properties, and water vapor supersaturation within the convective core regions of DCCs, all of which would assist to provide further clarity on the invigoration processes. Moreover, the thermodynamic and kinematic regimes under which aerosol-DCC interactions may be significant remain unresolved. Quantifying aerosol impacts on DCCs is further complicated because small-scale perturbations in large-scale vertical velocity, relative humidity, and other meteorological factors, such as wind shear and atmospheric instability, can potentially affect DCC intensity in a manner comparable to aerosol-induced changes (e.g., Fan et al., 2009; Storer et al., 2010; Grant and van den Heever, 2015; Lebo, 2018; Dagan et al., 2020; Park and van den Heever, 2022). Disentangling aerosol impacts on DCCs from those driven by meteorological factors is therefore difficult (e.g., Varble et al., 2023).

[c1] ~~the importance of these mechanisms relative to other DCC forcing~~

To accurately assess the contribution of aerosols to DCC properties, a variety of techniques and methods have been developed from both modeling and observational perspectives. On the modeling side, a range of statistical methods and modeling frameworks have been established, including the simple factor separation approach (van den Heever and Cotton, 2007; Grant and van den Heever, 2014), more sophisticated statistical emulators (Lee et al., 2011; Johnson et al., 2015; Wellmann et al., 2018; Park and van den Heever, 2022), and the piggybacking approach (Grabowski, 2015). These techniques have achieved some success in separating aerosol effects from the impacts of other forcing factors on DCC development. [c2]Though individual modeling studies have quantified aerosol effects on DCCs, it is important to note that there remains significant disagreement between these studies, even in the sign of effects, largely due to variations in model configurations and the methods used to analyze them (Varble et al., 2023). [c3]From the observational side, achieving this separation remains a longstanding challenge. The majority of observational studies have used multivariable models or basic machine learning approaches to mitigate potential confounding bias arising from meteorological covariates (e.g., Li et al., 2011; Storer et al., 2014; Veals et al., 2022; Zang et al., 2023). Nevertheless, it is important to emphasize that these methods can merely estimate the association or correlation between aerosols and DCCs, and proving correlation does not imply causation. Therefore, to gain a more thorough understanding of the underlying causal relationships and effects of aerosols on DCCs - or the absence of such effects - advanced statistical techniques are essential. Furthermore, it is vital to employ comprehensive, high-resolution observations of DCCs and aerosols to capture these intertwined physical processes and identify potential "fingerprints" of aerosol-DCC invigoration.

[c2] *Text added.*

[c3] ~~However, f~~

This study presents a novel statistical investigation into the aerosol-DCC interactions by applying causal machine learning methods to comprehensive observational datasets. The goal is to provide observational evidence of the aerosol casual effects on DCC intensity [c4], whether through invigoration or enervation. The datasets we used were collected during the TRacking Aerosol Convection interactions ExpeRiment (TRACER; Jensen et al., 2023) in Houston-Galveston, operated by the Department of Energy (DOE) Atmospheric Radiation Measurement (ARM) Climate Research Facility (Mather and Voyles, 2013). We focus on DCCs occurring during the summer months in 2022 from June to September, the TRACER Intensive Operational

[c4] ~~(either invigoration or enervation)~~

Period (IOP), as the synoptic conditions show less variation during this time interval and additional measurements of cloud, aerosol, and atmospheric profiling are available. To address the challenge of untangling the effects of aerosols from meteorological variables and estimating the aerosol causal effects, we employ a well-established causal model, g-computation (Robins, 1986), in combination with a Self-Organizing Map (SOM) approach (Kohonen, 1990). The SOM is used to identify synoptic regimes conducive to isolated DCCs, thereby minimizing the impact of large-scale ascents on their interactions with aerosols (Wang et al., 2022a). G-computation is chosen since it stands as a powerful model that facilitates the estimation of causal effects and exhibits versatility in handling a broad spectrum of sample sizes, making it particularly well-suited for studies with a limited sample size (e.g., Le Borgne et al., 2021). Furthermore, its flexibility allows us to model the relationship of interest using the statistical models of our choice (e.g., Chatton et al., 2020). [c5]In general, g-computation requires the identification of three types of variables for causal analysis: the exposure variable, the outcome variable, and the confounder variable(s). These variables are described in Table 1 and further explained in Section 3. This study marks the first application of the g-computation model to investigate aerosol-cloud interactions.

[c5] *Text added.*

2 Instrumentation and Datasets

2.1 DCC properties

As the first step in the investigation, we employ a Lagrangian framework to detect the formation and propagation of DCC rainfall cores and quantify their convective characteristics throughout their lifecycle. The term "DCC rainfall cores" typically refers to the convective regions in DCCs with heavy rainfall rates at the surface with a maximum value exceeding 10 mm/hr (e.g., Wang et al., 2018; Zhang et al., 2021). The maximum height of these cores can serve as a proxy for [c1]the maximum updraft [c2]velocity, as it correlates closely with the ability of updrafts in convective regions to lift large hydrometeors to higher altitudes, resulting in deeper convective systems (e.g., Heymsfield et al., 2010; Liu and Zipser, 2013; Guo et al., 2018). [c3]Note that this assumption neglects the possibility that aerosols may directly influence cloud microphysical processes (e.g., collision-coalescence, riming), which could, in turn, affect radar reflectivity and, consequently, the DCC ETH. Quantifying such influence is challenging in the absence of in-situ observations of the cloud microphysical and dynamical properties (e.g., hydrometeor phase/size distribution, updraft velocity). The reliance on this proxy also stems from the lack of direct measurements of convective vertical velocity for DCCs investigated here, a significant limitation not only for this study but also for many previous observational studies. Nevertheless, using ETH as a proxy allows for comparison of our findings with prior studies, which is valuable for the scientific community and for providing modeling constraints on simulations of the aerosol-DCC interactions.

[c1] *Text added.*
[c2] ~~strength~~
[c3] *Text added.*

More specifically, we tracked the trajectory of DCC rainfall cores using TINT (TINT Is Not TITAN [Thunderstorm Identification, Tracking Analysis and Nowcasting; Dixon and Wiener, 1993), a convective cell tracking algorithm developed by Raut et al. (2021). Building upon our prior research (Wang et al., 2024), we have effectively used this algorithm to analyze the level-II data (NOAA, 1991) from the S-band Doppler weather radar KHGX-Houston at 1-km horizontal resolution within a

domain of 400 km × 400 km centered around the radar location. As a result, we have generated a comprehensive tracked DCC rainfall core dataset for the TRACER IOP during the summer of 2022 (Wang et al., 2024).

In that study and the current one, DCC rainfall cores are defined using radar observations as contiguous areas where the 2-km radar reflectivity (Z) is greater than 10 dBZ, the lower limit for rain echo detection by NEXRAD radar systems, and the maximum 2-km Z value exceeds 40 dBZ (Anagnostou, 2004; Moroda et al., 2021). Note that different reflectivity thresholds varying from 30 to 40 dBZ have been selected for studying DCC convective cores in various climate conditions, depending on the objectives of the studies (e.g., Giangrande et al., 2023; Gupta et al., 2024). Additionally, these cores must exhibit a 30-dBZ echo top height (ETH) exceeding 5 km above ground level at some point during their lifetime to exclude the [c1] shallow convection [c2]cells, aligning with a similar definition proposed by Dixon and Wiener (1993). Further details regarding additional criteria for identifying and tracking these rainfall cores can be found in Texts S1 and S3 in the supporting information and in Wang et al. (2024). [c3]Note that using fixed thresholds may potentially influence the selection of DCCs investigated in the study, particularly in conditions where DCCs contain fewer raindrops due to the presence of a large number of background aerosols.

[c4]The first identification of the DCC rainfall core using the tracking algorithm signifies the initiation of surface rainfall associated with the DCC core. The tracking algorithm can no longer identify the core once the DCC ceases to produce moderate precipitation (maximum 2-km $Z < 40$ dBZ), marking the termination of the convective stage. In other words, the tracked lifetime of the cores excludes the initiation stage of non-precipitating cumulus clouds[c5], [c6] the dissipation stage of non-precipitating anvil clouds[c7], and the lightly precipitating periods during either stage. [c8] Table 2 details the number of DCC rainfall cores tracked and considered in each scenario.

The DCC intensity is quantified using the maximum 30-dBZ ETH of the tracked core as the primary indicator (e.g., Liu and Zipser, 2013; Guo et al., 2018). Additionally, some studies have used the maximum height of the 10-dBZ or 15-dBZ echo as proxies for cloud depth and convective updraft strength (e.g., Hu et al., 2019; Veals et al., 2022). Therefore, to test the sensitivity of the results to our assumed proxy, we also consider the maximum 15-dBZ ETH, calculated using the KHGX-Houston radar data, as a secondary indicator of convective intensity.

2.2 Meteorological variables

Meteorological conditions are crucial in shaping the formation and evolution of DCCs and may co-vary with aerosol properties, complicating the accurate quantification of aerosol-DCC interactions (e.g., Lee et al., 2008; Storer et al., 2010; Grant and van den Heever, 2015; Lebo, 2018; Dagan et al., 2020; Park and van den Heever, 2022; Zang et al., 2023; Varble et al., 2023). These meteorological variables or convective indices, influencing both aerosol activation and convective updraft strength, are termed "confounders" or "confounding variables" in causal inference (Jesson et al., 2021), and introduce the potential for spurious associations.

The convective indices analyzed in this study include convective available potential energy (CAPE), lifting condensation level (LCL), level of neutral buoyancy (LNB), environmental lapse rate (ELR) between 3 km and the surface (ELR_3), ELR between 6 km and 3 km (ELR_6), low-level vertical wind shear from the surface to 5 km (LWS), and low-level mean relative humidity below 5 km (RH). These variables have been identified in previous studies as the most influential meteorological

[c1] ~~presence of~~
[c2] *Text added.*
[c3] *Text added.*
[c4] ~~Note that t~~
[c5] *Text added.*
[c6] ~~and~~
[c7] *Text added.*
[c8] ~~Given the defined criteria and these important caveats, Figure 1 shows the locations of tracks corresponding to DCC rainfall cores formed within a 20 km radius of the TRACER main site (M1) at La Porte, TX, where comprehensive aerosol and meteorological measurements were collected. Additionally, Figure S1 (in the supporting informa-~~

factors altering the impacts of aerosols on convective updrafts and precipitation because these factors regulate the kinematic and microphysical processes in DCCs and the kinematic-microphysical feedback (e.g., Khain et al., 2008; Khain, 2009; Nishant et al., 2019; Fan et al., 2009; Tao et al., 2012; Storer et al., 2010, 2014; Varble, 2018; Wang et al., 2020a; Veals et al., 2022; Sun et al., 2023; Masrour and Rezazadeh, 2023).

To quantify these convective indices, measurements from the ARM balloon-borne sounding system (SONDE) launched at the M1 site are used. Radiosondes were typically launched four times a day at approximately 0530, 1130, 1730, and 2330 UTC during the TRACER campaign, with additional launches at 1900, 2030 and 2200 UTC on enhanced operational days (as listed in Table S1, in the supporting information). These radiosondes provide in situ measurements of atmospheric thermodynamic state profiles, wind speed, and wind direction. To address the sensitivity of these variable calculations to the choice of initial parcel conditions, three scenarios are considered. These scenarios involve lifting different air parcels to initiate a convective cloud: the surface-based parcel (*sfc*), the most unstable parcel (*mu*), and the mixed-layer parcel (*mix*). Detailed information on these calculations can be found in Wang et al. (2020b). [c1]Note that, in the calculations, we assume that the parcel undergoes undiluted ascent in a pseudo-adiabatic process (neglecting hydrometeor loading).

[c1] *Text added.*

Note that, in addition to the convective indices mentioned above, other factors such as entrainment rate (Abbott and Cronin, 2021; Peters et al., 2023) may also be important in regulating the aerosol-DCC interactions; however, no direct measurements of these quantities are available from TRACER. Therefore, these factors are not included in the analysis. The potential biases in the quantification of the aerosol causal effects due to these exclusions will be discussed in Section 4.6.

2.3 Surface aerosol measurements

The Aerosol Observing System (AOS; Uin et al., 2019) within the ARM mobile facility (AMF; Miller et al., 2016) was used for *in situ* aerosol measurements at the surface.

The dual-column CCN counter (Column A and Column B) was used to determine CCN number concentrations (N_{ccn}). This instrument measures the number and size of activated aerosol particles for each column at a specific supersaturation (SS) level. Particle size, after humidification, can be measured between 0.75-10 μm, and the range of particle number concentration measurement depends on the SS caused by the growth kinetics of activated particles. Column A has varying SS setpoints between 0% and 1% at a frequency of 1.5 hours, while Column B has a fixed SS setpoint of 0.35%. Due to the unavailability of Column B data at the time of the study, only Column A data were considered. The dataset used includes the number concentration of CCN at SS setpoints of 0.1%, 0.2%, 0.4%, 0.6%, 0.8%, and 1%, which are referred to as N_{ccn01}, N_{ccn02}, N_{ccn04}, N_{ccn06}, N_{ccn08}, and N_{ccn1}, respectively. Note that these measurements were bias-corrected based on a CCN closure study using methods developed by Petters and Kreidenweis (2007). As direct measurements of SS in convective cloud updrafts are not available (i.e., updraft SS is unknown), we consider all six parameters as potential predictors (individually) in the causal model.

Moreover, the total aerosol number concentrations including ultrafine particles [c2]($<$ 100 nm in diameter) in the nucleation and Aitken mode along with larger, accumulation mode aerosols are considered. The total aerosol number concentrations have the potential to influence DCC evolution, assuming that these particles may be activated as CCN in DCC updrafts in which

[c2] *Text added.*

a range of SS values may be present (e.g., Politovich and Cooper, 1988; Benmoshe, 2010). These quantities were measured by the condensation particle counter (CPC) installed as part of the ARM AOS (Singh and Kuang, 2024). Two types of CPC instruments were used in the AOS: ultrafine CPC instruments (CPCU) and fine mode CPC instruments (CPCF). The CPCU counts aerosol particles with diameters ranging from 3 to 3,000 nm (N_{ufp}), while CPCF counts aerosol particles with diameters ranging from 10 to 3,000 nm (N_{cn}).

[c1] The N_{cn} and N_{ufp} were measured at a temporal resolution of 1 minute, N_{ccn} at various SSs had two measurements per hour, and radiosondes, used to derive meteorological parameters, were launched four to seven times per day. To synchronize the two datasets, we employ two commonly used methods from previous studies to explore the sensitivity of results to the averaging process. One approach entails averaging the aerosol properties over a 1-hour period following the launch of a radiosonde (post-sounding averaging; e.g., Veals et al., 2022). The second method involves utilizing a 1-hour period preceding the initial identification of the rainfall cores, representing the aerosol conditions before the detection of precipitation at the surface (prior-rain averaging).

Based on a two-sample t-test (Welch, 2005), the differences between the distributions of the aerosol properties derived using the post-sounding averaging and the prior-rain averaging are statistically insignificant. This is true for all aerosol properties considered in this study. In addition, the median values of the aerosol parameters from these two averaging methods are also comparable, with relative differences ranging from 2% (N_{ccn02}) to 23% (N_{ccn01}). Similar results are found when comparing the variability of aerosol properties within the 1-hour averaging period, showing a consistent median value of the standard deviation for these parameters across all the DCC samples.

2.4 Pairing environmental variables with tracked DCCs

In order to establish causal relationships between aerosol and DCCs and facilitate calculations using g-computation, we align environmental variables (aerosol and meteorology) with tracked DCC properties. This is achieved by identifying DCC rainfall cores that form within 6 hours after launching each sounding, within a maximum distance of 50 km from the M1 site. The DCC tracking results are then averaged to represent the mean DCC properties for each corresponding sounding. [c2] More specifically, in terms of ETH, we identify the maximum ETH throughout a tracked DCC lifetime (one ETH for one DCC), then we average these ETHs to represent the mean ETH of these qualified DCCs. The specifics of the number of samples are detailed in Table 2.

[c3] The choice of a 6-hour time gap and a 50 km distance threshold as the upper limit represents a compromise between capturing representative environmental conditions and maintaining a sufficient sample size. We do want to emphasize the possibility of substantial temporal and spatial variability in the thermodynamic conditions around the M1 site. Local phenomena such as sea breeze, bay breeze, urban effects, and other factors may complicate the extent to which the environmental measurements at the M1 site represent the actual air mass injected into the DCCs (e.g., Rapp et al., 2024; Wang et al., 2024)

[c4] To account for the heterogeneous and evolving nature of meteorological conditions that may impact DCC development, we evaluate the spatial and temporal scales of meteorological influences on DCC rainfall core characteristics through sensitivity tests. These tests involve examining DCC rainfall cores initially identified within a radius of 20 km, 30 km, 40 km, and 50

[c1] ~~These aerosol properties (N_{ccn} at various SSs, N_{cn}, and N_{ufp}) were measured at a temporal resolution of 1 minute or less, while the radiosondes, used to derive the meteorological parameters, were launched four to seven times per day.~~

[c2] *Text added.*

[c3] ~~The choice of a 6-hour time gap and a 50 km distance threshold as the upper limit ensures the description of environmental conditions in close proximity in space and time to the early~~

km from the M1 site, considering two different groups of soundings: those launched within 4 hours and those within 6 hours before the initial identification of the DCC rainfall cores.

Given the temporal and spatial constraints of the current observations, the purpose of these tests is to strike the best possible balance between accurately characterizing the initial conditions where DCCs are embedded with the available observations and maintaining a sample size that optimizes the performance of the causal model.

Note that various pairing methods have been used in prior observational studies on aerosol-DCC interaction with the goal of expanding the sample size. One approach involves searching for a sounding launch within a specific time period preceding the identification of each tracked DCC within a defined domain (Veals et al., 2022). This increases the number of samples to be equal to the number of tracked DCCs, in contrast to our original method where the number of samples is equivalent to the number of sounding launches. It is crucial to acknowledge that different DCCs may correspond to the same sounding profiles in the Veals et al. (2022) method, limiting the natural variability of the pre-convection environment across different cases. Additionally, this lack of variability violates one of the assumptions of the g-computation model (i.e., stable unit treatment value assumption), which will be detailed in Section 3.4. Therefore, the subsequent analysis is exclusively conducted on datasets generated from the original method of using the mean properties of DCC rainfall cores tracked within 4 or 6 hours after the launch of each sounding.

3 Aerosol-DCC Causal Framework

To assess the potential impacts of aerosols on DCC ETH, a framework consisting of a three-step methodology is developed, incorporating the use of SOM and the g-computation model, as depicted in Figure 1.

In the first step (Figure 1a), we use the SOM method (Section 3.1) to classify the synoptic weather regimes with the aim of singling out DCC cases occurring within the context of weak synoptic-scale forcing. This choice serves to mitigate the potential influence of large-scale ascent on the evolution of DCCs. [c1] In other words, we aim to exclude large-scale, dynamically-driven convective clouds, such as mesoscale convective systems, since the aerosol effect may be overwhelmed by meteorological forcing (Chakraborty et al., 2016; Storer et al., 2010). The characteristics of the synoptic regimes over the Houston-Galveston region, details of the SOM setup, training process, and further information on the SOM method can be found in Wang et al. (2022a).

The second step (Figure 1b) involves the preparation of data for the g-computation model, with a focus on determining the exposure, confounding, and outcome variables (Sections 3.2 and 3.3). The terms "exposure" and "outcome" refer to the central variables of interest, where the exposure is believed to causally influence the outcome, and we aim to estimate this effect. If a variable affects both exposure and outcome variables, it is called a "confounder" or "confounding variable". In the context of this study, the potential exposure variables refer to aerosol properties such as N_{ccn} at various SSs, N_{cn}, or N_{ufp}, while the outcome variables refer to DCC properties such as 30-dBZ ETH or 15-dBZ ETH. The confounding variables refer to convective indices that may influence both DCC and aerosol properties such as CAPE.

Finally, in the last step (Figure 1c), the g-computation model is used to estimate the aerosol causal effects on DCC ETH (Section 3.4). This analysis involves predicting the outcome variables under different hypothetical scenarios wherein the rele-

[c1] ~~This is important given our focus on assessing aerosol effects on convective and buoyancy-driven updrafts, rather than on synoptic-scale, meteorological contributions to the convective updrafts.~~

vant confounding variables are held constant. Following the established terminology, these scenarios are hereafter referred to as counterfactual states (e.g., Hernan, 2004; Naimi et al., 2017). Specifically, we consider two counterfactual states: the polluted state, assuming that all DCCs are exposed to aerosols, and the clean state, assuming that none of the DCCs are exposed to aerosols. By comparing the predicted DCC ETH between these two counterfactual states, we can provide unbiased estimates of the causal effects of aerosols on DCC ETH.

3.1 Minimizing the influence of variability in synoptic-scale forcing

In this subsection, we describe the first step in which we use an unsupervised machine learning technique, SOM, to categorize synoptic weather patterns in the Houston-Galveston area (Figure 1a). The purpose of this step is to focus on DCC-aerosol relationships while minimizing the influence of synoptic-scale ascents such as those that are associated with strong synoptic-scale troughs and onshore winds.

In our prior studies (Wang et al., 2022a), we identified three main synoptic patterns in the Houston-Galveston region using the SOM approach, including a pre-trough, a post-trough, and an anticyclonic regime. The input data for SOM were 700-hPa geopotential height anomalies (recorded at 0000 UTC) from the European Centre for Medium-Range Weather Forecasts (ECMWF) Reanalysis version 5 (ERA5; Hersbach et al., 2020) during the summer months (June to September) of 2010 to 2022. Among these regimes, the anticyclonic regime is the most frequent, representing 49% of all days across the 13-year dataset, occurring predominantly in July and August. The corresponding regime for each day during the TRACER IOP can be found in Figure S2 (in the supporting information).

During the anticyclonic regime, a high-pressure system typically resides over the Houston-Galveston area as the Bermuda High has shifted toward the west. The region is positioned on the inner eastern edge of a ridge at 500 hPa, and on the inner western edge of an anticyclonic system at 850 hPa. This configuration creates a stable synoptic background characterized by large-scale subsidence over the study area, weak horizontal winds throughout the troposphere, and moderate column water vapor content (Wang et al., 2022a). These conditions are favorable for the formation of locally-forced, isolated DCCs with minimal [c1]LWS and moderate low-level moistening (Wang et al., 2024). As such, this environment is conducive to studying the interactions between DCCs and aerosols. Conversely, the pre-trough and post-trough regimes are associated with large-scale trough intrusions and moisture transport from the Gulf of Mexico, which are more likely to promote organized convective clouds over the region that are primarily driven by large-scale dynamics (Wang et al., 2022a). Therefore, these specific cases are excluded from our study, aligning with our emphasis on evaluating aerosol impacts on [c2]locally-driven DCCs, which are comparatively less influenced by the large-scale ascent.

[c1] ~~wind shear~~

[c2] ~~buoyancy-driven~~

3.2 Determination of exposure variables

This subsection outlines the determination of exposure variables for the g-computation model. Given our potential exposure variables or predictors, namely aerosol or CCN number concentrations at various SS levels, we aim to identify the most relevant aerosol parameters, impacting the DCC ETH. In other words, the selected exposure variables are those that demonstrate a significant association with DCC ETH.

To achieve that, we evaluate the performance of a simple linear regression (SLR) model when attempting to predict DCC ETH using each aerosol parameter individually. The *P*-value of each SLR model is assessed, indicating the statistical significance of the associations between ETH and aerosol parameters.

Note that since the g-computation calculation in the next step requires a binary exposure variable, the aerosol parameters are transformed into a binary distribution (0 or 1). Cases with N_{ccn} at various SSs, N_{cn}, or N_{ufp} above the median value are categorized as polluted cases with a scaled value of 1, while cases below the median value are classified as clean cases with a scaled value of 0. This transformation also helps address potential biases associated with the N_{ccn} measurements/calculations during TRACER since the exposure state is defined relative to a bulk statistical parameter (median value) which minimizes the dependence on individual measurement uncertainty. Several tests have been conducted to assess the sensitivity of the results to the clean-polluted separation threshold by using aerosol number concentrations less than the 40^{th} percentile for clean and higher than the 60^{th} percentile for polluted. The valid models remain the same, and similar causal effects are shown compared to the original setting. For simplicity, the following analysis uses the median value for the separation and the other thresholds are not shown.

Figure 2 illustrates the *P*-values resulting from each fitted model, with 30-dBZ ETH and 15-dBZ ETH as the outcome variable and each aerosol parameter (N_{ccn} at various SSs, N_{cn}, or N_{ufp}) as the predictor (derived from the two averaging methods described above). A *P*-value below 0.05 signifies a statistically significant association between the predictor and outcome variables. Only predictors demonstrating a *P*-value below 0.05 are considered as exposure variables in the subsequent causal analysis.

The most notable feature from Figure 2 is that only a small fraction (20 out of 128, accounting for 16%) of the SLR models are statistically significant. This result suggests that, in the majority of scenarios, the aerosol number concentration is not a reliable influencer of changes in DCC ETH, suggesting limited favorable conditions for aerosol loading to impact DCC updraft strength. Among the valid SLR models ($P < 0.05$), most of them use N_{cn} or N_{ufp} as the predictor variable. This implies that aerosol loading potentially influences convective updraft intensity if all particles are activated in those updrafts, including the ultrafine particles. Whether a certain level of SS or a range of SS values can be reached within those updrafts to activate all the aerosol particles is not observed. The actual SS values may depend on meteorological conditions such as atmospheric instability and moisture availability, in addition to updraft strength. This underscores the importance of considering these meteorological conditions (like the convective indices defined above) as confounding variables in the causal model.

3.3 Identification of confounders

In this subsection, our primary objective is to identify a specific set of confounding variables from a range of convective indices introduced in Section 2.2. To achieve this, we assess the Pearson correlation coefficients (*R*) between 30-dBZ ETH/15-dBZ ETH and selected convective indices, as delineated in Table 3 and shown in Figure 3.

Positive *R*-values between 0.2 and 0.4 are evident when examining the relationship between LNB, $CAPE_{mu}$, LCL, or ELR_3 and 30-dBZ ETH. The positive association between $CAPE_{mu}$ and 30-dBZ ETH can primarily be attributed to the direct impact of CAPE on the maximum potential velocity of updrafts, independent of entrainment and hydrometer loading effects

(Weisman and Klemp, 1984; Kirkpatrick et al., 2011). This relationship finds support in observations across diverse climate regions, including Darwin, Australia (Kumar et al., 2013), the Sierras de Córdoba mountain range (Veals et al., 2022), and the central Amazon (Wang et al., 2019). This robust association is also present when using surface parcels but diminishes with mixed-layer parcels (Table S2, in the supporting information). Additionally, LNB shows weak, positive correlation with both 30-dBZ ETH and 15-dBZ ETH, since it is highly correlated to CAPE (Figure 3).

Concerning LCL, its impact on 30-dBZ ETH can be explained by its previously demonstrated positive correlation with the width of updrafts at cloud base (McCaul and Cohen, 2002; Mulholland et al., 2021). In other words, a higher LCL tends to promote wider boundary-layer updrafts. These wider updrafts are more likely to evolve into expansive and deeper updraft cores within DCCs since they experience less dilution of buoyancy due to entrainment compared to narrower updraft cores. Consequently, this leads to a higher 30-dBZ ETH. Similarly, a steeper ELR_3 is closely linked to a higher LCL (R = 0.9, Figure 3), and subsequently, a higher 30-dBZ ETH. This steeper ELR_3 also corresponds to a "fatter" buoyancy profile (Zipser and LeMone, 1980), where CAPE is concentrated at lower levels. An air parcel accelerates more rapidly through these levels, reducing the exposure time for entrainment and other processes (Wang et al., 2020b). Therefore, a higher 30-dBZ ETH may be expected.

LWS is another essential factor governing DCC updraft intensity and regulating aerosol-DCC interactions, particularly in organized DCCs (e.g., Fan et al., 2009; Baidu et al., 2022). However, in the specific isolated DCC environment studied here, it has no association with 30-dBZ ETH, but does have a weak, negative correlation with 15-dBZ ETH. Therefore, LWS is excluded (included) as a confounding variable when the 30-dBZ ETH (15-dBZ ETH) is considered as the outcome variable in the causal model.

Overall, LNB, CAPE, LCL, and ELR_3 exhibit weak to moderate R-values across various scenarios, making them suitable potential covariates for predicting 30-dBZ ETH alongside aerosol properties. However, high correlation is found between LNB and CAPE (R = 0.9, Figure 3) as higher values of CAPE indicate greater atmospheric instability, allowing air parcels to rise to higher altitudes, thus potentially higher LNB. Similarly, strong correlation is also exhibited between ELR_3 and LCL (R = 0.9, Figure 3), which can be attributed to their shared relationship with temperature variations in the lower atmosphere. To address multicollinearity concerns, only one variable from each pair is selected as a confounding variable, which can otherwise lead to increased variance in estimated coefficients within the g-computation model. Further discussion on multicollinearity is presented in Text S4 of the supporting information. Note that opting for fewer confounders also has the advantage of partially addressing challenges related to the [c1] robustness of the causal model given the relatively limited sample size in this study.

[c1] ~~accuracy~~

Finally, CAPE and ELR_3 are chosen due to their higher R-values with 30-dBZ ETH compared to their counterparts. Following a similar logic, CAPE and LWS are selected as confounders when the 15-dBZ ETH is used as the outcome variable in the causal model. Moreover, these selected confounding variables exhibit a stronger association with aerosol parameters compared to other convective indices (Figure 3). Similar findings are reported in previous studies by Varble (2018). Using the surface and mixed-layer parcel, a consistent conclusion is drawn (Figures S3 and S4, in the supporting information).

3.4 G-computation causal model

G-computation, along with g-methods in general (Robins, 1986), is widely utilized across various fields and has garnered significant attention in the scientific community for causal analysis, particularly in epidemiology (e.g., Mooney et al., 2021; Chatton et al., 2020). This model is a statistical technique utilized to estimate the causal effect of an exposure or condition in the presence of a set of confounders in observational studies.

The accuracy of the g-computation model relies on several key assumptions. These assumptions include:

1. Temporality: It assumes that the exposure occurs before the outcome. In our study, we use aerosol properties observed prior to the detection of convective rainfall echos at the surface for all DCC cases, satisfying this requirement.

2. Stable unit treatment value: It assumes that the exposure of one observation to the exposure variable does not affect the potential outcomes of other observations. While the first initiated DCCs over a specific region may modify the environmental conditions for subsequent DCCs, our study primarily focuses on isolated DCC cases with short durations and limited cloud to cloud interactions. The DCC cases also occurred on different days during the IOP, leading us to expect minimal impact of one DCC on another DCC.

3. Positivity: It assumes that there is sufficient variability in the exposure and outcome variables for each confounder in the data. Our dataset shows considerable variability in both aerosol and meteorological variables (Figures 4 and 7), which satisfies this assumption.

4. Ignorability: We assume that all major confounding variables are included in the data. Critical quantities known to influence ETH, such as CAPE and LWS, are explicitly included or discussed, [c1] to a large extent, supporting this assumption. While variables like entrainment rate and vertical velocity also likely confound aerosol and DCC properties, their exclusion in this study is dictated by the absence of direct measurements during TRACER. To address potential biases arising from unobserved confounders, a comprehensive discussion is provided in Section 4.6.

[c1] ~~sufficiently~~

The g-computation model consists of three steps used to estimate the causal effect of an exposure (Figure 1):

1. The outcome (Y, ETH in this case) is modeled as a function of the exposure (A, aerosol number concentration in this case) and relevant confounders (V; CAPE and ELR_3/LWS in this case) using a statistical model such as logistic, linear regression, or a predictive machine learning model (E(Y|A, V)), commonly known as the "Q-model".

2. The fitted Q-model is used to predict counterfactual outcomes for each observation under each exposure scenario (whether exposed to high concentration of aerosols or not). This is done by setting A = 1 (polluted) and subsequently A = 0 (clean) into the Q-model fit to obtain predicted outcomes for these two settings.

3. Finally, the average causal effect is calculated by taking the difference between the average counterfactual outcomes under the exposed and unexposed conditions.

We describe each step in detail in the following subsections.

3.4.1 Fit a Q-model

The first step in the g-computation process involves fitting a statistical Q-model to the dataset. Given the limited number of DCC cases in our study, we have chosen to use the multiple linear regression (MLR) model, which is suitable for analyzing relatively small datasets. In our case, the MLR model includes the outcome variable, Y, which represents the 30-dBZ (15-dBZ ETH), and the exposure variable, A, which represents N_{cn} or N_{ufp}. We also include two confounding variables, V, which are V1 = CAPE, V2 = ELR_3 for Y = 30-dBZ ETH and V1 = CAPE, V2 = LWS for Y = 15-dBZ ETH.

The MLR model can be expressed as follows: Y = b0 + b1A + b2V1 + b3V2. Here, b0 represents the value of Y when all independent variables (exposure and confounding variables) are equal to zero, or it can be interpreted as the residual term. The coefficients b1, b2, and b3 are the estimated regression coefficients associated with the exposure and confounding variables.

[c1] We perform standardization on all the confounding variables. This standardization process transforms the variables so that they have a mean of 0 and a standard deviation of 1. It is achieved by subtracting the mean of each variable from each observation and then dividing by its standard deviation. This procedure helps mitigate the impact of different units and ranges of the variables, allowing for meaningful comparisons of the regression coefficients on the same scale.

[c2] We run model diagnostics to ensure the validity, reliability, and interpretability of the fitted MLR model as well as ensuring the robustness of coefficients. This is achieved by examining the key assumptions (i.e., linearity, homoscedasticity, normality, independence, and multicollinearity) of the MLR models as described in Text S4 in the supporting information. Overall, all valid scenarios presented in Section 3.2 satisfy these assumptions. In addition, we also calculated the adjusted R^2 values, the 95% confidence intervals for each independent variable (Table S4 in the supporting information). The adjusted R^2 values are generally below 0.5 and rarely increase even when all the potential confounders discussed in section 2.2 are included. This result infers that other confounding variables, beyond those included or discussed here, likely exist but are not accounted for. These variables may not have been measured or discovered to have a relationship with the outcome variables which will be discussed in section 4.6. Additionally, the small sample size may contribute to the low adjusted R^2, as high variability in the outcome variable can artificially suppress it.

3.4.2 Estimate counterfactual outcomes and average causal effects

The next step involves estimating the counterfactual outcomes under different conditions and calculating the average causal effect of the aerosol number concentration on ETH.

First, we use the fitted MLR model to predict the ETH values under both clean and polluted conditions for each observation in the dataset. This is done by setting the aerosol number concentration (exposure variable) to 0 (A=0, in the Q-model) for clean conditions and 1 (A=1, in the Q-model) for polluted conditions for each observation in the data set, while keeping the other confounders at their observed values.

Second, we calculate the causal effect by comparing the counterfactual predicted outcomes under the two aerosol conditions. This involves taking the difference between the predicted ETH values under polluted conditions and clean conditions for

[c1] ~~To further address potential multicollinearity issues between the covariates, w~~

[c2] ~~One of the important steps is to evaluate the performance of the MLR model, which can lend confidence in the causal effect estimated in the next step. This is achieved by examining the key assumptions (i.e., linearity, homoscedasticity, normality, independence, and multicollinearity) of the MLR models as described in Text S4 in the supporting information. Overall, all valid~~

each observation. To estimate the average causal effect on ETH across the entire dataset, we weight these differences by the proportions of observations in the polluted and clean groups.

4 Houston-Galveston environments and results from the causal model

In this section, we first provide an overview of the characteristics of the DCC properties and their associated aerosol and meteorological conditions in the Houston-Galveston region. Then, we present results from the causal analyses and discuss potential uncertainties of the results.

4.1 DCC properties and their associated environmental conditions

In Figure 4, we illustrate the distributions of selected convective indices representative of the pre-convective conditions. During the selected DCC days, the influence of anticyclonic large-scale flow leads to moderate low-level moistening, resulting in medium-to-high low-level RH (mean RH values below 5 km) of approximately 70% (Figure 4o). This moistening causes air parcels to saturate quickly at lower levels when lifted, leading to a relatively low mean LCL of 1 km (Figures 4g-i), although this value is higher compared to the LCL values in more humid conditions, such as an oceanic environment with a mean low-level RH of 80% (Wang et al., 2020b). The LCL is in close proximity to the LFC, with a smaller median difference of 100 m when using the most-unstable parcel and a larger difference of 600 m when using a mixed-layer parcel (Figures 4j-l). Consequently, the convective inhibition (CIN_{mu}) is relatively low, with a median value of -0.7 J/kg (not shown).

Under these conditions, (adiabatically) lifted parcels can ascend to significant heights, even reaching the tropopause, with a mean LNB_{mu} of 14.6 km (Figure 4d). When considering mixed-layer parcels, the mean value of LNB_{mix} decreases to 13.9 km as expected (Figure 4f). This environment allows for the accumulation of significant $CAPE_{mu}$ throughout the troposphere, with a median value of approximately 3,407 J/kg (Figure 4a). There are limited changes in CAPE values when using the surface parcel in the calculation compared to $CAPE_{mu}$ (Figure 4b), which implies that most of the most-unstable parcels are from near surface levels. Under such circumstances, using surface aerosol measurements to represent the in-cloud aerosol properties may result in reduced uncertainty compared to applying the same assumption to study elevated DCCs. The LWS is relatively weak, with a mean value of 5.7 ms^{-1} (Figure 4n), compared to [c1] LWS values that support the initiation of organized convective systems (Baidu et al., 2022).

[c1] ~~wind shear~~

The distributions of convective properties associated with DCCs initiated under such meteorological conditions are illustrated in Figure 5. In this demonstration, the selected DCC cases are those identified within a 50 km radius from the ARM M1 site. The definitions of these properties can be found in Text S2 in the supporting information. These tracked DCC rainfall cores show intense rainfall rates, exhibiting a mean maximum 2-km *Z* of 54 dBZ (Figure 5a). The maximum 30-dBZ ETH for half of these cores extends above 7 km (Figure 5b). These cores are small in size, with their maximum area having a median value of approximately 52 km^2 during their lifetime (Figure 5c), confirming their more isolated nature. Most of these rainfall cores form in the afternoon hours with a peak in the number of cores initiating around 2000 UTC, corresponding to 1500 local time (Figure 5d). This observation confirms that these cases are predominantly locally driven under weak synoptic-forcing and influenced by surface heating and/or sea-breeze circulations (Wang et al., 2022a). It is therefore no surprise that these cores

propagate at a relatively slow speed of 5 ms^{-1} (Figure 5e) and have a relatively short duration of less than an hour (51 min, Figure 5f). The influence of aerosol number concentrations on these locally-driven DCC rainfall cores is expected to be more discernible compared to DCCs with significant large-scale forcing, given the limited large-scale ascent and minimal convection organization in such cases.

[c1] Figure 6 illustrates the spatial distribution of DCC properties, showing a notable cluster along a line perpendicular to the coastline and northwest of the M1 site. This pattern can potentially be attributed to the interplay between sea breeze, bay breeze, and urban heat island-induced circulations, which may create a conducive environment for DCC initiation and/or collisions (Mejia et al., 2024). Such events appear to result in larger cell areas, as depicted in Figure 6c, and slightly longer lifetimes compared to cells located outside this zone (Figure 6f), consistent with findings by Hahn et al. (2024). Additionally, it is observed that these cells tend to initiate later in the day (Figure 6d), aligning with the timing of sea and bay breeze propagation and their convergence with urban heat island circulations in this region. Note that the spatiotemporal heterogeneity of these precipitation cores adds complexity to our study, as it relies on point measurements of environmental variables. While this approach is a practical solution given the absence of a comprehensive measurement network during TRACER, it highlights the need for long-term field campaigns with enhanced instrumentation to achieve better spatial coverage across regions with complex multiscale forcings.

[c1] *Text added.*

Throughout the DCC days, the Houston-Galveston region experienced diverse aerosol number concentrations. As shown in Figure 7, the distribution of aerosol number concentrations spans a considerable range with a prominent peak at smaller number concentration bins. The mean values of these SS-determined distributions are significantly different according to results from a t-test, except for N_{ccn1} and N_{ccn08}. More specifically, this environment exhibits mean total aerosol number concentrations of 7,332 cm^{-3} for N_{cn} and 10,683 cm^{-3} for N_{ufp} during the study period (Figures 7g, h), showing high pollution levels. The most polluted instances occurred in mid-July (e.g., July 12, 13) and mid-August (e.g., August 10, 11, 17), exceeding the 95th percentile values of the distributions shown in Figure 7.

In addition, the Houston-Galveston region is found to have a unique combination of different aerosol species during the summer months (Figure S5, in the supporting information), according to the aerosol mass concentration measurements at the M1 site. The predominant aerosol type measured is total organics, constituting 49% (2.24 μgm^{-3}) of the total aerosol mass concentration, followed by sulfate at 34% (1.54 μgm^{-3}), ammonium at 13% (0.61 μgm^{-3}), nitrate at 3% (0.14 μgm^{-3}), and chloride at $< 1\%$ (0.03 μgm^{-3}). This broad spectrum of aerosol species and their mass concentration is indicative of various emission sources, including both anthropogenic (e.g., from city, ships, refineries; Rivera et al., 2010; Wallace et al., 2018) and natural emissions (e.g., from agricultural activities, vegetation; Bean et al., 2016; Yoon et al., 2021) from nearby and/or distant locations.

4.2 Average aerosol causal effects on DCC ETH

Figure 8 illustrates the estimated average causal effect of aerosol number concentration on 30-dBZ ETH and 15-dBZ ETH, for all scenarios and varying distances (20 to 50 km) from the M1 site. The valid scenarios are indicated by the white hatch lines, which are determined in Section 3.2. The confounding meteorological variables are calculated using the most unstable

parcel in this figure, and the post-sounding aerosol averaging method is used. The findings reveal a positive average causal effect for N_{cn} and N_{ufp}, when all aerosol particles are activated in convective updrafts. It implies that higher aerosol number concentration values correspond to an increase in 30-dBZ ETH within DCCs, thereby suggesting a stronger convective updraft in polluted conditions compared to that in clean conditions. However, the expected causal effects of aerosols on the 30-dBZ ETH show only moderate variations when using different exposure variables in the causal model, ranging between 0.6 km to 2.2 km. The mean aerosol causal effect across these valid scenarios is 1.0 km or 13% of the average 30-dBZ ETH. We observe similar results when using 15-dBZ ETH as the outcome variable and when using different air parcels for calculating confounding variables, as illustrated in Table 4.

[c1]Interestingly, when conducting causal analysis on the "invalid" scenarios, the estimated average aerosol causal effects are mostly negative (Figure 8), highlighting the potential for contradictory results when a different exposure variable is used. Even for the “valid” scenarios, the significance of the estimated causal effects is challenged by the inconsistent 95% confidence intervals for the coefficients of the exposure variables in the fitted MLR models (Table S4 in the supporting information). Specifically, the 95% confidence intervals for the exposure variables sometimes cross 0, making it difficult to conclude that the exposures have a clear and meaningful influence on the outcome. This finding is consistent with the relatively small or minimal causal effects observed for these scenarios in Figures 8 and 9, which are likely to fall into the uncertainty range of the measurements or related to the sampling methods we used.

In a separate test, we ran the causal model without any confounders, and we found that the estimated mean aerosol causal effects on 30-dBZ ETH increased to 1.4 km, which is 0.4 km larger than when including two confounders. These results highlight the importance of considering confounders while quantifying aerosol impacts on convective properties.

[c2]We also conducted a sensitivity test to examine whether the diurnal cycle affects the causal relationships between aerosol properties and ETH. The results indicate that the average causal effects are only 0.1 km lower than those presented in Figure 8, where the diurnal cycle was not controlled for. This suggests that the diurnal cycle has a limited influence on the aerosol causal effects on ETH under the specific environmental conditions of this study.

Note that the observational findings presented in this study do not unequivocally lend support to or negate the previously proposed warm-phase invigoration pathway. The role of in-cloud SS is vital in determining the occurrence of warm-phase invigoration within DCCs (e.g., Romps et al., 2023). Unfortunately, direct *in situ* measurements of SS within convective updrafts remain unavailable, despite estimates using aircraft measurements for limited climate and vertical velocity regimes (e.g., Politovich and Cooper, 1988; Pinsky and Khain, 2002; Korolev and Mazin, 2003; Prabha et al., 2011; Romps et al., 2023). The aerosol invigoration effect in our study is substantiated based on the assumption that in-cloud SS exceeds a certain threshold to activate all aerosol particles. In essence, the results do not directly support warm-phase invigoration unless in-cloud SS is measured or estimated in line with our assumptions. [c3]In addition, the high concentrations of larger aerosol particles observed under the assessed conditions (Figure 7) raise doubts about the likelihood of all ultrafine particles being activated. This, in turn, challenges our hypothesis that aerosols may influence DCC ETH under the assumption that all ultrafine particles are activated.

[c1] ~~Interestingly, when conducting causal analysis on the invalid scenarios, the estimated average aerosol causal effects are mostly negative (Figure 8). This highlights the importance of evaluating the causal model or any prediction model used in similar studies, as without this evaluation, contradictory results may be obtained.~~

[c2] *Text added.*

[c3] *Text added.*

Similarly, the presented causal effects do not conclusively confirm or reject the possibility of other hypothesized aerosol invigoration mechanisms (e.g., cold-phase, entrainment-humidity invigoration). As shown in Figure 5b, a substantial portion of the 30-dBZ ETH associated with the studied rainfall cores extends beyond 5 km. Consequently, the observed positive causal effects of aerosols under specific conditions suggest potential evidence of cold-phase invigoration or partitioning between warm- and cold-phase invigoration. However, to fully support these invigoration mechanisms, we need to further assess the relative importance of additional latent heat release and hydrometeor loading (e.g., Igel and van den Heever, 2021). It requires crucial supporting measurements of hydrometeor and latent heating profiles in the convective updraft region, which were not available during the majority of the TRACER IOP. Moreover, while entrainment is found to alter aerosol-DCC interactions (e.g., Peters et al., 2023), the absence of vital, direct measurements of convective vertical velocity, presents a challenge in evaluating the significance of this process.

In summary, we demonstrate a causal link between aerosol number concentrations and ETH using various observational data sets through a novel application of the g-computation model. However, to gain a comprehensive understanding of the plausible pathways driving aerosol-induced effects on ETH necessitates advanced instrumentation and specific field campaign designation, which are capable of capturing SS levels, vertical velocity within updrafts and understanding the intricate dynamics and microphysical processes occurring within DCCs.

4.3 Impacts of the sea-breeze circulations on aerosol causal effects

The ARM M1 site is located in close proximity to Galveston Bay (6 km) and the Gulf of Mexico (50 km), frequently experiencing Bay- and Gulf-breeze circulations (simplified as sea-breeze circulations in the following text) during the summer months (Wang et al., 2024). Despite focusing on cases within the anticyclonic regime to exclude large-scale ascent contributions to the development of DCCs, sea-breeze fronts can still act as meso-scale forcing mechanisms, inducing upward motions within the boundary layer and influencing aerosol-DCC interactions.

Our recent study (Wang et al., 2024) indicates that at least 44% of the DCC rainfall cores analyzed here are associated with days that these circulations are present. In that study, we identified sea-breeze circulation days based on observations from NEXRAD, Geostationary Operational Environmental Satellites (GOES), and ARM surface meteorology data (e.g., wind fields, water vapor mixing ratio). Specifically, 64 sea-breeze circulation cases were determined during the TRACER IOP. As shown in Table 2, 38 rainfall cores, with a sounding launch within 6 hours prior to rainfall initiation, were tracked during these days within 50 km of the ARM M1 site in this study.

We applied the causal framework to DCCs that are associated with sea-breeze circulations, maintaining the same confounding variables since they showed moderate correlations with both outcome and exposure variables (R values ranging from 0.4 to 0.5). Figure 9 illustrates the causal effect on 30 dBZ ETH as the outcome variable. The mean causal effect observed is 1.4 km, which is higher than estimates for scenarios including all cases (Table 4). This increase could be due to the potential exclusion of confounding variables that are not major contributors to non-sea-breeze cases. One important variable could be boundary layer updrafts, which consistently increase at the leading edge of sea-breeze fronts as observed from the Doppler Lidar measurements (Wang et al., 2024). Since this observation is only available at the ARM M1 site and not for each tracked rainfall

core, it is challenging to include this confounding variable in the causal model. The exclusion of this confounding variable may lead to an overestimation of the causal effects of aerosols on ETH as discussed in the previous section.

Interestingly, we found more valid causal models (19) for the sea-breeze cases compared to scenarios including all cases. This suggests that the aerosol influence is a robust signal here, even though the extension of the ETH is not more than 15%. This robustness may be due to the coherent separation of clean versus polluted cases when using different exposure variables. This is supported by the observations that the DCC environment is much cleaner after the passage of sea-breeze fronts.

4.4 Average aerosol causal effects on precipitation intensity and area

In this subsection, we extend our causal framework to estimate the impacts of aerosols on precipitation intensity and area. Precipitation intensity is assessed using the maximum 2-km radar reflectivity, while precipitation area is evaluated based on the maximum area with 2-km $Z > 30$ dBZ of the tracked precipitation core throughout the cell life cycle. All steps in the causal framework remain the same for these applications, except the outcome variable is either maximum radar reflectivity or precipitation core area instead of ETH. The confounding variable considered in this analysis is only CAPE, as it is the only one that shows a correlation coefficient higher than 0.3 with both outcome and exposure variables.

Figure 10 presents the causal effects on the core area for different potential exposure variables. Only one causal model is valid, which corresponds to the scenario with DCCs identified within 30 km of the M1 site using N_{ccn} measured at SS of 0.8%. This finding implies that, only on rare occasions, aerosol number concentration impacts the precipitation core area expansion by approximately 39 km^2. Given the fact that this area expansion is only observed in limited scenarios, it is less conclusive compared to the effects of aerosols on DCC ETH.

Regarding the causal effects of aerosols on precipitation intensity, Figure 11 shows ten effective models, significantly more than those considering core area as the outcome variable. Although the mean causal effect across all valid scenarios is positive, the magnitude is around 2 dBZ, which falls within the uncertainty range of the NEXRAD radar (3 dBZ; Gou, 2003; Ryzhkov et al., 2005). Therefore, we cannot conclusively determine that aerosol loading results in heavier precipitation for the DCC cases evaluated in this study.

4.5 Sensitivity of the causal effect estimation

We explore the robustness of aerosol causal effect estimates by examining various factors that could influence the calculations. These factors include the data averaging period for aerosol measurements and the time gap between environmental measurements and DCC rainfall initiation [c1](e.g., Nelson et al., 2021; Fast et al., 2024).

[c1] *Text added.*

When using the prior-rain method for the aerosol averaging process, as shown in Figures 2b, d, we observe that the effective aerosol properties (exposure variables) remain consistent with those obtained using the post-sounding method (Figures 2a, c), involving N_{cn} and N_{ufp}. The mean aerosol effect on 30-dBZ ETH [c2]and 15-dBZ ETH is 1.1 km [c3]and 1.0 km, [c4]respectively, which aligns closely with the results obtained using the post-sounding aerosol averaging method (Table 4). These findings suggest that the causal model results have minimal sensitivity to the data averaging period for the measured aerosol properties used in this study.

[c2] *,*
[c3] *,*
[c4] *Text added.*

Regarding the influence of the time gap between measurements of DCC and environmental properties on the estimation of the aerosol causal effect, we exclude the cases when the nearest soundings were launched more than 4 hours before the initiation of DCC rainfall cores (Table 4). As shown in Table 4, the mean aerosol effect on 30-dBZ ETH/15-dBZ ETH across all valid scenarios is 1.2 km/1.2 km, only slightly higher than using 6-hour soundings.

The shorter the time difference, in theory, the more accurately the sounding measurement should represent the environment in which the DCCs are embedded. Therefore, these results reinforce the conclusion from previous sections, suggesting that aerosol invigoration is, for the most part, constrained, and requires all aerosol particles to be activated in convective updrafts if it is to be effective. However, the number of samples is reduced by approximately 20% when limiting our analysis to 4-hour soundings. Additionally, the percentage of cases heavily influenced by sea-breeze circulations also changes. These changes could all potentially impact the casual model results.

In summary, the assessment of aerosol causal effects appears independent of the timing of environmental measurements relative to the initiation of DCCs and the accuracy with which these measurements reflect the air ingested into the DCC updraft cores. Nonetheless, the collective findings indicate a restricted impact of aerosols on DCCs across all sensitivity tests conducted in the Houston-Galveston region under anticyclonic regimes.

4.6 Potential uncertainties in causal analysis

The g-computation model is a flexible and powerful technique, but its application to observational data necessitates careful consideration of assumptions and potential sources of bias. One major challenge when estimating the causal effect of an exposure is controlling for unobserved or unknown confounders (e.g., Barrowman et al., 2019; Hjellvik et al., 2019). The presence of unobserved/unknown confounders may cause the observed data distribution to be compatible with many contradictory causal explanations.

In this study, we have accounted for important confounders that could influence the aerosol-DCC interactions according to previous studies and also our evaluations, but there may still be some confounders that we did not observe or discover that could impact our results. For example, Peters et al. (2023) discovered that entrainment rate influences whether aerosols have an impact on DCCs. Additionally, the size of the updraft core in the boundary layer prior to the cloud formation is identified as a significant factor influencing the intensity of the subsequently developed DCCs (e.g., Morrison, 2017; Mulholland et al., 2021; Takahashi et al., 2023). However, direct measurements of these quantities were not available during TRACER and most other field campaigns aimed at observing the characteristics of deep convection. The lack of confounders in the causal model may possibly cause an overestimation of the aerosol causal effects. Nonetheless, even though all the confounders are observed, to balance the number of samples and the number of confounders in the causal model, these confounders may not all be included in the model (as discussed in Section 3.3).

Recently, several potential solutions have emerged that show promising results in overcoming this challenge (D'Amour, 2019; Peterson et al., 2023). For example, Liu et al. (2020) controlled for unobserved confounders in a novel manner by using double binary confounders that satisfy a nonlinear condition on the exposure. Various simulations show better estimation performance compared to the current approach. Such simulations will be considered in our future studies. [c1]In the absence of

[c1] *Text added.*

in-situ observations of cloud microphysical properties, the current analysis cannot account for any 'direct' effects of aerosols on ETH or cloud depth through microphysical processes. Neither does the study investigate the microphysical pathways through which aerosols may cause the changes in ETH. Such examinations require in-situ observations and/or high-resolution model simulations, which forms a key limitation of any study aiming to explore aerosol-DCC interactions using remote sensing retrievals alone.

5 Conclusions

This study introduces a novel application of the g-computation causal inference model to explore the causal effects of aerosols on the rainfall core properties of DCCs, aiming to provide evidence of aerosol invigoration or enervation. Leveraging the extensive observational dataset collected during the TRACER IOP (Jun. - Sep.) in the Houston-Galveston region, characterized by a diverse aerosol environment, we focus on examining isolated DCCs observed during this period in the anticyclonic regime.

To identify suitable DCCs for investigation, we establish an interpretable framework including a three-step process.

First, we exclude synoptic-scale system-driven cases by applying a regime classification of synoptic weather patterns using the SOM method. This step allows us to focus on locally driven cases under anticyclonic regimes, which are found to be more conducive to aerosol interactions in previous studies. The selected period is characterized by low [c1]LWS, limited large-scale uplift, and moderate humidity conditions, favoring predominantly isolated DCCs driven by local factors.

[c1] ~~shear~~

Second, we track DCC cases initiated within a certain distance from the M1 site using a Lagrangian framework based on NEXRAD data. This tracking process helps determine the properties of the DCC rainfall cores, which are identified as small in size (74 km^2 on average), slow propagating (5 ms^{-1} on average), and short-lived (51 min on average), with predominantly afternoon initiation likely influenced by surface heating flux and/or sea-breeze circulations. In particular, 44% of the DCC cells tracked occurred on sea-breeze days.

Finally, we use the g-computation model to assess the causal effect of aerosols on identified DCCs. Before implementing the model, we categorize observed variables into three groups: exposure, confounder, and outcome variables. The outcome variables, representing updraft strength, are 30-dBZ ETH or 15-dBZ ETH. From eight aerosol parameters (N_{ccn} at six SSs, N_{cn}, and N_{ufp}), we select exposure variables by evaluating the performance of SLR models, where the relationships between these variables and the outcome variables are fitted. Only a small fraction (16%) of the SLR models are valid, indicating that, in the majority of cases, aerosol loading is not [c2]robustly associated with [c3] DCC [c4]maximum ETH, suggesting insufficient effects of aerosols on DCC updraft velocity in these situations [c5]with the current sample sizes. For confounders, we identify two observed convective indices that covary with aerosol and DCC, (CAPE and ELR_3 for 30-dBZ ETH, CAPE and LWS for 15-dBZ ETH) and need to be considered when estimating aerosol effects. In the g-computation model, we initially fit a Q-model (MLR model in our case), where the outcome is modeled as a function of the exposure and relevant confounders. Subsequently, the fitted MLR model is employed to predict counterfactual outcomes for each observation under each exposure scenario (clean or polluted). Finally, the average causal effect is calculated by taking the difference between the average counterfactual outcomes under the clean and polluted conditions.

[c2] *Text added.*
[c3] ~~the evolution of~~
[c4] *Text added.*
[c5] *Text added.*

The major findings include:

1. After accounting for confounders, [c1]we observed a wide range of average causal effects of aerosols on DCC ETH, spanning from negative to positive values. In a small subset of models where aerosols were strongly linked to ETH, we detected a positive average causal effect, ranging from 0.7 to 1.2 km. These findings highlight the substantial uncertainty in the sign of aerosol impacts. Only under specific conditions might a more polluted environment lead to stronger convection compared to cleaner conditions, assuming all other factors remain equal. However, such conditions are difficult to achieve in the study region, where the activation of all ultrafine particles poses significant challenges.

2. When assessing the impacts of sea-breeze circulations on aerosol-DCC interactions, we found a slightly higher impact of aerosol number concentration on 30-dBZ ETH (0.4 km deepening) compared to the all-case scenario. This discrepancy could be due to the absence of major confounding variables (e.g., boundary layer dynamics) considered in the causal model for this scenario.

3. We also apply the causal framework to investigate the impact of aerosol loading on precipitation core area. [c2]Most models indicated positive average causal effects, suggesting an expansion of cell area in polluted cases. However, [c3]as only one model is deemed "valid," the robustness of this result needs further assessment. Moreover, regarding the influence of aerosols on maximum rainfall intensity, the observed effects fall within the range of radar measurement uncertainty.

4. The sensitivity analysis reveals minimal dependency on the choice of the proxy for updraft intensity, the temporal and spatial gaps between measurements of aerosol and DCC properties, the aerosol averaging period, and the types of originating air parcels used in calculating CAPE. In other words, these tests all show comparable causal effects of aerosols on 30-dBZ ETH.

[c4]Nevertheless, this study demonstrates the potential of using a causal model to evaluate the effects of aerosols on DCC properties, providing new insights into aerosol-convection interactions through observations. It also represents a step forward in addressing the challenges of disentangling aerosol-meteorological co-variability in these interactions. Additionally, this causal framework shows promise for broader applications, offering a valuable tool for exploring complex scientific questions across various disciplines.

Code and data availability.

1. ARM data can be downloaded from https://adc.arm.gov/discovery/#/
2. NEXRAD data is accessible at https://registry.opendata.aws/noaa-nexrad/
3. TINT package: https://github.com/openradar/TINT
4. [c5]Post-processed data: https://doi.org/10.5281/zenodo.14298966

[c1] ~~we observed a positive average causal effect of aerosols on DCC ETH, ranging from 0.7 to 1.2 km. This result suggests that in these particular scenarios, a stronger convective updraft may be expected in a more polluted condition compared to those in a clean condition, everything else being equal or similar. This influence is optimal when the SS levels in the convective updates support the activation of all aerosol particles injected.~~

[c2] ~~There is only one model that shows valid results, indicating an expansion of cell area in the polluted cases.~~

[c3] *Text added.*

[c4] ~~Nevertheless, this~~

5. [c6]Codes for running g-computation: https://doi.org/10.5281/zenodo.14299094

Author contributions. DW and MJ designed the study. DW conducted the analysis and wrote the manuscript. RK and TZ provided guidance on running the causal model. TS provided the aerosol dataset. SVDH, SG, and MJ reviewed the manuscript.

Competing interests. The authors have no conflicts of interest to declare.

690 *Acknowledgements.* This paper has been authored by employees of Brookhaven Science Associates, LLC, under Contract DE-SC0012704 with the U.S. Department of Energy (DOE). We would like to acknowledge the DOE Early Career Research Program for the funding support. We also would like to acknowledge support from the Atmospheric System Research (ASR) program, the Atmospheric Radiation Measurement (ARM) user facility, and the ARM TRACER operation and science teams. SV is supported by the DOE under DE-SC0021160. SG is supported by Argonne National Laboratory under U.S. DOE contract DE-AC02-06CH11357 and the ARM User Facility, funded by the
695 Office of Biological and Environmental Research in the U.S DOE Office of Science. We thank Maria Zawadowicz at Brookhaven National Lab for providing the calculated CCN number concentrations.

[c6] *Text*

References

Evaluating the calibrations of radars: A software approach, 31st InternationalConference on Radar Meteorology, Seattle, Washington, 2003.

Abbott, T. H. and Cronin, T. W.: Aerosol invigoration of atmospheric convection through increases in humidity, Science, 371, 83–85, https://doi.org/10.1126/science.abc5181, 2021.

Anagnostou, E. N.: A convective/stratiform precipitation classification algorithm for volume scanning weather radar observations, Meteorological Applications, 11, 291–300, https://doi.org/https://doi.org/10.1017/S1350482704001409, 2004.

Andreae, M. O., Rosenfeld, D., Artaxo, P., Costa, A. A., Frank, G., Longo, K. M., and Silva-Dias, M. A. F. d.: Smoking rain clouds over the Amazon, science, 303, 1337–1342, 2004.

Baidu, M., Schwendike, J., Marsham, J. H., and Bain, C.: Effects of vertical wind shear on intensities of mesoscale convective systems over West and Central Africa, Atmospheric Science Letters, 23, e1094, https://doi.org/https://doi.org/10.1002/asl.1094, 2022.

Barrowman, M., Peek, N., Lambie, M., Martin, G., and Sperrin, M.: How unmeasured confounding in a competing risks setting can affect treatment effect estimates in observational studies, BMC Med Res Methodol., 31, 166, https://doi.org/10.1186/s12874-019-0808-7, 2019.

Barth, M. C., Cantrell, C. A., Brune, W. H., Rutledge, S. A., Crawford, J. H., Huntrieser, H., Carey, L. D., MacGorman, D., Weisman, M., Pickering, K. E., Bruning, E., Anderson, B., Apel, E., Biggerstaff, M., Campos, T., Campuzano-Jost, P., Cohen, R., Crounse, J., Day, D. A., Diskin, G., Flocke, F., Fried, A., Garland, C., Heikes, B., Honomichl, S., Hornbrook, R., Huey, L. G., Jimenez, J. L., Lang, T., Lichtenstern, M., Mikoviny, T., Nault, B., O'Sullivan, D., Pan, L. L., Peischl, J., Pollack, I., Richter, D., Riemer, D., Ryerson, T., Schlager, H., Clair, J. S., Walega, J., Weibring, P., Weinheimer, A., Wennberg, P., Wisthaler, A., Wooldridge, P. J., and Ziegler, C.: The Deep Convective Clouds and Chemistry (DC3) Field Campaign, Bulletin of the American Meteorological Society, 96, 1281 – 1309, https://doi.org/10.1175/BAMS-D-13-00290.1, 2015.

Bean, J. K., Faxon, C. B., Leong, Y. J., Wallace, H. W., Cevik, B. K., Ortiz, S., Canagaratna, M. R., Usenko, S., Sheesley, R. J., Griffin, R. J., and Hildebrandt Ruiz, L.: Composition and Sources of Particulate Matter Measured near Houston, TX: Anthropogenic-Biogenic Interactions, Atmosphere, 7, https://doi.org/10.3390/atmos7050073, 2016.

Benmoshe, N.: Mechanisms of lightning formation in deep maritime clouds and hurricanes (The HAMP contribution), 2010.

Bony, S., Stevens, B., Coppin, D., Becker, T., Reed, K. A., Voigt, A., and Medeiros, B.: Thermodynamic control of anvil cloud amount, Proceedings of the National Academy of Sciences, 113, 8927–8932, https://doi.org/10.1073/pnas.1601472113, 2016.

Chatton, A., Le Borgne, F., and Leyrat, C.: G-computation, propensity score-based methods, and targeted maximum likelihood estimator for causal inference with different covariates sets: a comparative simulation study, Sci Rep, 10, https://doi.org/https://doi.org/10.1038/s41598-020-65917-x, 2020.

Chi, N.-H., Lien, R.-C., D'Asaro, E. A., and Ma, B. B.: The surface mixed layer heat budget from mooring observations in the central Indian Ocean during Madden–Julian Oscillation events, Journal of Geophysical Research: Oceans, 119, 4638–4652, https://doi.org/https://doi.org/10.1002/2014JC010192, 2014.

Dagan, G.: Equilibrium climate sensitivity increases with aerosol concentration due to changes in precipitation efficiency, Atmospheric Chemistry and Physics, 22, 15 767–15 775, https://doi.org/10.5194/acp-22-15767-2022, 2022.

Dagan, G., Stier, P., Christensen, M., Cioni, G., Klocke, D., and Seifert, A.: Atmospheric energy budget response to idealized aerosol perturbation in tropical cloud systems, Atmospheric Chemistry and Physics, 20, 4523–4544, https://doi.org/10.5194/acp-20-4523-2020, 2020.

D'Amour, A.: On Multi-Cause Approaches to Causal Inference with Unobserved Counfounding: Two Cautionary Failure Cases and A Promising Alternative, in: International Conference on Artificial Intelligence and Statistics, 2019.

Del Genio, A.: Representing the Sensitivity of Convective Cloud Systems to Tropospheric Humidity in General Circulation Models, Surv Geophys, 33, 637 – 656, https://doi.org/https://doi.org/10.1007/s10712-011-9148-9, 2012.

Dixon, M. and Wiener, G.: TITAN: Thunderstorm Identification, Tracking, Analysis, and Nowcasting—A Radar-based Methodology, Journal of Atmospheric and Oceanic Technology, 10, 785 – 797, https://doi.org/10.1175/1520-0426(1993)010<0785:TTITAA>2.0.CO;2, 1993.

Dye, J. E., Ridley, B. A., Skamarock, W., Barth, M., Venticinque, M., Defer, E., Blanchet, P., Thery, C., Laroche, P., Baumann, K., Hubler, G., Parrish, D. D., Ryerson, T., Trainer, M., Frost, G., Holloway, J. S., Matejka, T., Bartels, D., Fehsenfeld, F. C., Tuck, A., Rutledge, S. A., Lang, T., Stith, J., and Zerr, R.: An overview of the Stratospheric-Tropospheric Experiment: Radiation, Aerosols, and Ozone (STERAO)-Deep Convection experiment with results for the July 10, 1996 storm, Journal of Geophysical Research: Atmospheres, 105, 10 023–10 045, https://doi.org/https://doi.org/10.1029/1999JD901116, 2000.

Fan, J., Yuan, T., Comstock, J. M., Ghan, S., Khain, A., Leung, L. R., Li, Z., Martins, V. J., and Ovchinnikov, M.: Dominant role by vertical wind shear in regulating aerosol effects on deep convective clouds, Journal of Geophysical Research: Atmospheres, 114, https://doi.org/https://doi.org/10.1029/2009JD012352, 2009.

Fan, J., Rosenfeld, D., Zhang, Y., Giangrande, S. E., Li, Z., Machado, L. A. T., Martin, S. T., Yang, Y., Wang, J., Artaxo, P., Barbosa, H. M. J., Braga, R. C., Comstock, J. M., Feng, Z., Gao, W., Gomes, H. B., Mei, F., Pöhlker, C., Pöhlker, M. L., Pöschl, U., and de Souza, R. A. F.: Substantial convection and precipitation enhancements by ultrafine aerosol particles, Science, 359, 411–418, https://doi.org/10.1126/science.aan8461, 2018.

Fan, J., Zhang, Y., Li, Z., Hu, J., and Rosenfeld, D.: Urbanization-induced land and aerosol impacts on sea-breeze circulation and convective precipitation, Atmospheric Chemistry and Physics, 20, 14 163–14 182, https://doi.org/10.5194/acp-20-14163-2020, 2020.

Feng, Z., Leung, L. R., Hagos, S., Houze, R. A., Burleyson, C. D., and Balaguru, K.: More frequent intense and long-lived storms dominate the springtime trend in central US rainfall, Nature communications, 7, 1–8, 2016.

Geerts, B., Parsons, D., Ziegler, C. L., Weckwerth, T. M., Biggerstaff, M. I., Clark, R. D., Coniglio, M. C., Demoz, B. B., Ferrare, R. A., Gallus, W. A., Haghi, K., Hanesiak, J. M., Klein, P. M., Knupp, K. R., Kosiba, K., McFarquhar, G. M., Moore, J. A., Nehrir, A. R., Parker, M. D., Pinto, J. O., Rauber, R. M., Schumacher, R. S., Turner, D. D., Wang, Q., Wang, X., Wang, Z., and Wurman, J.: The 2015 Plains Elevated Convection at Night Field Project, Bulletin of the American Meteorological Society, 98, 767 – 786, https://doi.org/10.1175/BAMS-D-15-00257.1, 2017.

Giangrande, S. E., Biscaro, T. S., and Peters, J. M.: Seasonal controls on isolated convective storm drafts, precipitation intensity, and life cycle as observed during GoAmazon2014/5, Atmospheric Chemistry and Physics, 23, 5297–5316, https://doi.org/10.5194/acp-23-5297-2023, 2023.

Grabowski, W. W.: Untangling Microphysical Impacts on Deep Convection Applying a Novel Modeling Methodology, Journal of the Atmospheric Sciences, 72, 2446 – 2464, https://doi.org/10.1175/JAS-D-14-0307.1, 2015.

Grabowski, W. W. and Morrison, H.: Do Ultrafine Cloud Condensation Nuclei Invigorate Deep Convection?, Journal of the Atmospheric Sciences, 77, 2567 – 2583, https://doi.org/10.1175/JAS-D-20-0012.1, 2020.

Grant, L. D. and van den Heever, S. C.: Aerosol-cloud-land surface interactions within tropical sea breeze convection, Journal of Geophysical Research: Atmospheres, 119, 8340–8361, https://doi.org/https://doi.org/10.1002/2014JD021912, 2014.

Grant, L. D. and van den Heever, S. C.: Cold Pool and Precipitation Responses to Aerosol Loading: Modulation by Dry Layers, Journal of the Atmospheric Sciences, 72, 1398 – 1408, https://doi.org/10.1175/JAS-D-14-0260.1, 2015.

Guo, J., Liu, H., Li, Z., Rosenfeld, D., Jiang, M., Xu, W., Jiang, J. H., He, J., Chen, D., Min, M., and Zhai, P.: Aerosol-induced changes in the vertical structure of precipitation: a perspective of TRMM precipitation radar, Atmospheric Chemistry and Physics, 18, 13 329–13 343, https://doi.org/10.5194/acp-18-13329-2018, 2018.

Gupta, S., Wang, D., Giangrande, S. E., Biscaro, T. S., and Jensen, M. P.: Lifecycle of updrafts and mass flux in isolated deep convection over the Amazon rainforest: insights from cell tracking, Atmospheric Chemistry and Physics, 24, 4487–4510, https://doi.org/10.5194/acp-24-4487-2024, 2024.

Hernan, M.: A definition of causal effect for epidemiological research, J Epidemiol Community Health, 58, 265–271, 2004.

Hersbach, H., Bell, B., Berrisford, P., Hirahara, S., Horányi, A., Muñoz-Sabater, J., Nicolas, J., Peubey, C., Radu, R., Schepers, D., et al.: The ERA5 global reanalysis, Quarterly Journal of the Royal Meteorological Society, 146, 1999–2049, 2020.

Heymsfield, G. M., Tian, L., Heymsfield, A. J., Li, L., and Guimond, S.: Characteristics of Deep Tropical and Subtropical Convection from Nadir-Viewing High-Altitude Airborne Doppler Radar, Journal of the Atmospheric Sciences, 67, 285 – 308, https://doi.org/10.1175/2009JAS3132.1, 2010.

Hjellvik, V., De Bruin, M. L., Samuelsen, S. O., Karlstad, O., Andersen, M., Haukka, J., Vestergaard, P., de Vries, F., and Furu, K.: Adjusting for unmeasured confounding using validation data: Simplified two-stage calibration for survival and dichotomous outcomes, Statistics in Medicine, 38, 2719–2734, https://doi.org/https://doi.org/10.1002/sim.8131, 2019.

Hu, J., Rosenfeld, D., Ryzhkov, A., Zrnic, D., Williams, E., Zhang, P., Snyder, J. C., Zhang, R., and Weitz, R.: Polarimetric Radar Convective Cell Tracking Reveals Large Sensitivity of Cloud Precipitation and Electrification Properties to CCN, Journal of Geophysical Research: Atmospheres, 124, 12 194–12 205, https://doi.org/https://doi.org/10.1029/2019JD030857, 2019.

Igel, A. L. and van den Heever, S. C.: Invigoration or Enervation of Convective Clouds by Aerosols?, Geophysical Research Letters, 48, e2021GL093 804, https://doi.org/https://doi.org/10.1029/2021GL093804, 2021.

Jensen, M. P., Petersen, W. A., Bansemer, A., Bharadwaj, N., Carey, L. D., Cecil, D. J., Collis, S. M., Genio, A. D. D., Dolan, B., Gerlach, J., Giangrande, S. E., Heymsfield, A., Heymsfield, G., Kollias, P., Lang, T. J., Nesbitt, S. W., Neumann, A., Poellot, M., Rutledge, S. A., Schwaller, M., Tokay, A., Williams, C. R., Wolff, D. B., Xie, S., and Zipser, E. J.: The Midlatitude Continental Convective Clouds Experiment (MC3E), Bulletin of the American Meteorological Society, 97, 1667 – 1686, https://doi.org/10.1175/BAMS-D-14-00228.1, 2016.

Jensen, M. P., Flynn, J. H., Judd, L. M., Kollias, P., Kuang, C., Mcfarquhar, G., Nadkarni, R., Powers, H., and Sullivan, J.: A Succession of Cloud, Precipitation, Aerosol, and Air Quality Field Experiments in the Coastal Urban Environment, Bulletin of the American Meteorological Society, 103, 103 – 105, https://doi.org/10.1175/BAMS-D-21-0104.1, 2022.

Jesson, A., Mindermann, S., Gal, Y., and Shalit, U.: Quantifying Ignorance in Individual-Level Causal-Effect Estimates under Hidden Confounding, in: Proceedings of the 38th International Conference on Machine Learning, edited by Meila, M. and Zhang, T., vol. 139 of *Proceedings of Machine Learning Research*, pp. 4829–4838, PMLR, https://proceedings.mlr.press/v139/jesson21a.html, 2021.

Johnson, J. S., Cui, Z., Lee, L. A., Gosling, J. P., Blyth, A. M., and Carslaw, K. S.: Evaluating uncertainty in convective cloud microphysics using statistical emulation, Journal of Advances in Modeling Earth Systems, 7, 162–187, https://doi.org/https://doi.org/10.1002/2014MS000383, 2015.

Khain, A., Rosenfeld, D., and Pokrovsky, A.: Aerosol impact on the dynamics and microphysics of deep convective clouds, Quarterly Journal of the Royal Meteorological Society: A journal of the atmospheric sciences, applied meteorology and physical oceanography, 131, 2639–2663, 2005.

Khain, A. P.: Notes on state-of-the-art investigations of aerosol effects on precipitation: a critical review, Environmental Research Letters, 4, 015 004, https://doi.org/10.1088/1748-9326/4/1/015004, 2009.

Khain, A. P., BenMoshe, N., and Pokrovsky, A.: Factors Determining the Impact of Aerosols on Surface Precipitation from Clouds: An Attempt at Classification, Journal of the Atmospheric Sciences, 65, 1721 – 1748, https://doi.org/10.1175/2007JAS2515.1, 2008.

Kirkpatrick, C., McCaul, E. W., and Cohen, C.: Sensitivities of Simulated Convective Storms to Environmental CAPE, Monthly Weather Review, 139, 3514 – 3532, https://doi.org/10.1175/2011MWR3631.1, 2011.

Kohonen, T.: The self-organizing map, Proceedings of the IEEE, 78, 1464–1480, https://doi.org/10.1109/5.58325, 1990.

Kollias, P., McFarquhar, G., Oue, M., van den Heever, S., Logan, T., Bruning, E., Lombardo, K., Kumjian, M., Lebo, Z., Shaw, R., Roberts, G., , DeMott, P., McCluskey, C., Patnaude, R., Dzambo, A., Wolde, M., Nguyen, C., Lawson, P., Bruintjes, R., Lamer, K., Luke, E., Treserras, B. P., Chandrasekaran, V., Snyder, J., Bodine, D., Ranjbar, K., Nichman, L., Roux, E., Tsai, P., Wolf, C., Junyent, F., Mages, Z., Barr, J., Zhu, Z., McKeown, K., Brunner, K., Singewald, D., Souza, J., Rosky, E., Allwayin, N., Patil, S., Hu, Y., Xia, Z., Qiao, Y., Huang, Y., Miller, M., Denny, B., Ascher, B., and Weiss, S.: Experiment of Sea Breeze Convection, Aerosols, Precipitation and Environment (ESCAPE), Bulletin of the American Meteorological Society, in press, 2024.

Korolev, A. V. and Mazin, I. P.: Supersaturation of Water Vapor in Clouds, Journal of the Atmospheric Sciences, 60, 2957 – 2974, https://doi.org/10.1175/1520-0469(2003)060<2957:SOWVIC>2.0.CO;2, 2003.

Kumar, V. V., Protat, A., May, P. T., Jakob, C., Penide, G., Kumar, S., and Davies, L.: On the Effects of Large-Scale Environment and Surface Types on Convective Cloud Characteristics over Darwin, Australia, Monthly Weather Review, 141, 1358 – 1374, https://doi.org/10.1175/MWR-D-12-00160.1, 2013.

Le Borgne, F., Chatton, A., and Léger, M.: G-computation and machine learning for estimating the causal effects of binary exposure statuses on binary outcomes, Sci Rep, 11, https://doi.org/https://doi.org/10.1038/s41598-021-81110-0, 2021.
Lebo, Z.: A Numerical Investigation of the Potential Effects of Aerosol-Induced Warming and Updraft Width and Slope on Updraft Intensity in Deep Convective Clouds, Journal of the Atmospheric Sciences, 75, 535 – 554, https://doi.org/10.1175/JAS-D-16-0368.1, 2018.
Lebo, Z. J. and Seinfeld, J. H.: Theoretical basis for convective invigoration due to increased aerosol concentration, Atmospheric Chemistry and Physics, 11, 5407–5429, https://doi.org/10.5194/acp-11-5407-2011, 2011.
Lee, L. A., Carslaw, K. S., Pringle, K. J., Mann, G. W., and Spracklen, D. V.: Emulation of a complex global aerosol model to quantify sensitivity to uncertain parameters, Atmospheric Chemistry and Physics, 11, 12 253–12 273, https://doi.org/10.5194/acp-11-12253-2011, 2011.
Lee, S. S., Donner, L. J., Phillips, V. T. J., and Ming, Y.: The dependence of aerosol effects on clouds and precipitation on cloud-system organization, shear and stability, Journal of Geophysical Research: Atmospheres, 113, https://doi.org/https://doi.org/10.1029/2007JD009224, 2008.
Li, Z., Niu, F., Fan, J., Liu, Y., Rosenfeld, D., and Ding, Y.: Long-term impacts of aerosols on the vertical development of clouds and precipitation, Nature Geoscience, 4, 888–894, 2011.
Liu, C. and Zipser, E.: Regional variation of morphology of organized convection in the tropics and subtropics, Journal of Geophysical Research: Atmospheres, 118, 453–466, https://doi.org/https://doi.org/10.1029/2012JD018409, 2013.
Liu, L., Hou, L., and Yu, Y.: A novel method for controlling unobserved confounding using double confounders, BMC Med Res Methodol, 20, https://doi.org/https://doi.org/10.1186/s12874-020-01049-0, 2020.
Long, C. N., DelGenio, A., May, P., Gustafson, W., McFarlane, S., Houze, R., Minnis, P., Jakob, C., Schumacher, C., Jensen, M., Vogelmann, A., Klein, S., Wang, Y., and etc: AMIE (ARM MJO Investigation Experiment): Observations of the Madden–Julian oscillation for modeling studies science plan, DOE/ARM Tech. Rep. DOE/SC-ARM-10-007, 20, https://www.arm.gov/publications/programdocs/doe-sc-arm-10-007.pdf, 2011.
Marinescu, P. J., van den Heever, S. C., Heikenfeld, M., Barrett, A. I., Barthlott, C., Hoose, C., Fan, J., Fridlind, A. M., Matsui, T., Miltenberger, A. K., Stier, P., Vie, B., White, B. A., and Zhang, Y.: Impacts of Varying Concentrations of Cloud Condensation Nuclei on Deep Convective Cloud Updrafts—A Multimodel Assessment, Journal of the Atmospheric Sciences, 78, 1147 – 1172, https://doi.org/10.1175/JAS-D-20-0200.1, 2021.
Martin, S. T., Artaxo, P., Machado, L., Manzi, A. O., Souza, R. A. F., Schumacher, C., Wang, J., Biscaro, T., Brito, J., Calheiros, A., Jardine, K., Medeiros, A., Portela, B., de Sá, S. S., Adachi, K., Aiken, A. C., Albrecht, R., Alexander, L., Andreae, M. O., Barbosa, H. M. J., Buseck, P., Chand, D., Comstock, J. M., Day, D. A., Dubey, M., Fan, J., Fast, J., Fisch, G., Fortner, E., Giangrande, S., Gilles, M., Goldstein, A. H., Guenther, A., Hubbe, J., Jensen, M., Jimenez, J. L., Keutsch, F. N., Kim, S., Kuang, C., Laskin, A., McKinney, K., Mei, F., Miller, M., Nascimento, R., Pauliquevis, T., Pekour, M., Peres, J., Petäjä, T., Pöhlker, C., Pöschl, U., Rizzo, L., Schmid, B., Shilling, J. E., Dias, M. A. S., Smith, J. N., Tomlinson, J. M., Tóta, J., and Wendisch, M.: The Green Ocean Amazon Experiment (GoAmazon2014/5) Observes Pollution Affecting Gases, Aerosols, Clouds, and Rainfall over the Rain Forest, Bulletin of the American Meteorological Society, 98, 981 – 997, https://doi.org/10.1175/BAMS-D-15-00221.1, 2017.
Masrour, P. F. and Rezazadeh, M.: Aerosol-cloud-precipitation interaction during some convective events over southwestern Iran using the WRF model, Atmospheric Pollution Research, 14, 101 667, https://doi.org/https://doi.org/10.1016/j.apr.2023.101667, 2023.
Mather, J. H. and Voyles, J. W.: The ARM Climate Research Facility: A review of structure and capabilities, Bulletin of the American Meteorological Society, 94, 377–392, 2013.
McCaul, E. W. and Cohen, C.: The Impact on Simulated Storm Structure and Intensity of Variations in the Mixed Layer and Moist Layer Depths, Monthly Weather Review, 130, 1722 – 1748, https://doi.org/10.1175/1520-0493(2002)130<1722:TIOSSS>2.0.CO;2, 2002.
Miller, M. A., Nitschke, K., Ackerman, T. P., Ferrell, W. R., Hickmon, N., and Ivey, M.: The ARM Mobile Facilities, Meteorological Monographs, 57, 9.1 – 9.15, https://doi.org/10.1175/AMSMONOGRAPHS-D-15-0051.1, 2016.
Moncrieff, M. W.: The Multiscale Organization of Moist Convection and the Intersection of Weather and Climate, pp. 3–26, American Geophysical Union (AGU), ISBN 9781118670392, https://doi.org/https://doi.org/10.1029/2008GM000838, 2010.
Mooney, S. J., Shev, A. B., Keyes, K. M., Tracy, M., and Cerd, M.: G-Computation and Agent-Based Modeling for Social Epidemiology: Can Population Interventions Prevent Posttraumatic Stress Disorder?, American Journal of Epidemiology, 191, 188–197, https://doi.org/10.1093/aje/kwab219, 2021.
Moroda, Y., TSUBOKI, K., SATOH, S., NAKAGAWA, K., USHIO, T., and SHIMIZU, S.: Structure and Evolution of Precipitation Cores in an Isolated Convective Storm Observed by Phased Array Weather Radar, Journal of the Meteorological Society of Japan. Ser. II, 99, 765–784, https://doi.org/10.2151/jmsj.2021-038, 2021.
Morrison, H.: An Analytic Description of the Structure and Evolution of Growing Deep Cumulus Updrafts, Journal of the Atmospheric Sciences, 74, 809 – 834, https://doi.org/10.1175/JAS-D-16-0234.1, 2017.
Mulholland, J. P., Peters, J. M., and Morrison, H.: How Does LCL Height Influence Deep Convective Updraft Width?, Geophysical Research Letters, 48, e2021GL093 316, https://doi.org/https://doi.org/10.1029/2021GL093316, e2021GL093316 2021GL093316, 2021.
Naimi, A., Cole, S., and Kennedy, E.: An introduction to g methods, Int J Epidemiol, 46, 756–762, https://doi.org/10.1093/ije/dyw323, 2017.
Nishant, N., Sherwood, S., and Geoffroy, O.: Aerosol-induced modification of organised convection and top-of-atmosphere radiation, npj Clim Atmos Sci, 2, https://doi.org/10.1038/s41612-019-0089-1, 2019.
NOAA: Doppler radar meteorological observations, Part C, WSR-88D products and algorithms, Tech. Rep. Rep. FCM-H11C-1991, Office of the Federal Coordinator for Meteorological Services and Supporting Research, available from National Climatic Data Center, 1991.
Park, J. M. and van den Heever, S. C.: Weakening of tropical sea breeze convective systems through interactions of aerosol, radiation, and soil moisture, Atmospheric Chemistry and Physics, 22, 10 527–10 549, https://doi.org/10.5194/acp-22-10527-2022, 2022.
Peters, J. M., Lebo, Z. J., Chavas, D. R., and Su, C.-Y.: Entrainment Makes Pollution More Likely to Weaken Deep Convective Updrafts Than Invigorate Them, Geophysical Research Letters, 50, e2023GL103 314, https://doi.org/https://doi.org/10.1029/2023GL103314, 2023.
Peterson, R. L., Vock, D. M., and Koopmeiners, J. S.: Estimating Longitudinal Causal Effects with Unobserved Noncompliance Using a Semi-Parametric G-computation Algorithm, 2023.

Petters, M. D. and Kreidenweis, S. M.: A single parameter representation of hygroscopic growth and cloud condensation nucleus activity, Atmospheric Chemistry and Physics, 7, 1961–1971, https://doi.org/10.5194/acp-7-1961-2007, 2007.
Pinsky, M. B. and Khain, A. P.: Effects of in-cloud nucleation and turbulence on droplet spectrum formation in cumulus clouds, Quarterly Journal of the Royal Meteorological Society, 128, 501–533, https://doi.org/https://doi.org/10.1256/003590002321042072, 2002.
Polavarapu, R. and Austin, G.: A review of the GARP Atlantic tropical experiment (gate), Atmosphere-Ocean, 17, 1–13, https://doi.org/10.1080/07055900.1979.9649047, 1979.
Politovich, M. K. and Cooper, W. A.: Variability of the Supersaturation in Cumulus Clouds, Journal of Atmospheric Sciences, 45, 1651 – 1664, https://doi.org/10.1175/1520-0469(1988)045<1651:VOTSIC>2.0.CO;2, 1988.
Prabha, T. V., Khain, A., Maheshkumar, R. S., Pandithurai, G., Kulkarni, J. R., Konwar, M., and Goswami, B. N.: Microphysics of Pre-monsoon and Monsoon Clouds as Seen from In Situ Measurements during the Cloud Aerosol Interaction and Precipitation Enhancement Experiment (CAIPEEX), Journal of the Atmospheric Sciences, 68, 1882 – 1901, https://doi.org/10.1175/2011JAS3707.1, 2011.
Prein, A. F., Rasmussen, R. M., Wang, D., and Giangrande, S. E.: Sensitivity of organized convective storms to model grid spacing in current and future climates, Philosophical Transactions of the Royal Society A: Mathematical, Physical and Engineering Sciences, 379, 20190 546, https://doi.org/10.1098/rsta.2019.0546, 2021.
Prein, A. F., Ge, M., Valle, A. R., Wang, D., and Giangrande, S. E.: Towards a Unified Setup to Simulate Mid-Latitude and Tropical Mesoscale Convective Systems at Kilometer-Scales, Earth and Space Science, 9, e2022EA002 295, https://doi.org/https://doi.org/10.1029/2022EA002295, e2022EA002295 2022EA002295, 2022.
Ramos-Valle, A. N., Prein, A. F., Ge, M., Wang, D., and Giangrande, S. E.: Grid Spacing Sensitivities of Simulated Mid-Latitude and Tropical Mesoscale Convective Systems in the Convective Gray Zone, Journal of Geophysical Research: Atmospheres, 128, e2022JD037 043, https://doi.org/https://doi.org/10.1029/2022JD037043, e2022JD037043 2022JD037043, 2023.
Raut, B. A., Jackson, R., Picel, M., Collis, S. M., Bergemann, M., and Jakob, C.: An adaptive tracking algorithm for convection in simulated and remote sensing data, Journal of Applied Meteorology and Climatology, 60, 513–526, 2021.
Reid, J. S., Maring, H. B., Narisma, G. T., van den Heever, S., Girolamo, L. D., Ferrare, R., Lawson, P., Mace, G. G., Simpas, J. B., Tanelli, S., Ziemba, L., van Diedenhoven, B., Bruintjes, R., Bucholtz, A., Cairns, B., Cambaliza, M. O., Chen, G., Diskin, G. S., Flynn, J. H., Hostetler, C. A., Holz, R. E., Lang, T. J., Schmidt, K. S., Smith, G., Sorooshian, A., Thompson, E. J., Thornhill, K. L., Trepte, C., Wang, J., Woods, S., Yoon, S., Alexandrov, M., Alvarez, S., Amiot, C. G., Bennett, J. R., Brooks, M., Burton, S. P., Cayanan, E., Chen, H., Collow, A., Crosbie, E., DaSilva, A., DiGangi, J. P., Flagg, D. D., Freeman, S. W., Fu, D., Fukada, E., Hilario, M. R. A., Hong, Y., Hristova-Veleva, S. M., Kuehn, R., Kowch, R. S., Leung, G. R., Loveridge, J., Meyer, K., Miller, R. M., Montes, M. J., Moum, J. N., Nenes, A., Nesbitt, S. W., Norgren, M., Nowottnick, E. P., Rauber, R. M., Reid, E. A., Rutledge, S., Schlosser, J. S., Sekiyama, T. T., Shook, M. A., Sokolowsky, G. A., Stamnes, S. A., Tanaka, T. Y., Wasilewski, A., Xian, P., Xiao, Q., Xu, Z., and Zavaleta, J.: The Coupling Between Tropical Meteorology, Aerosol Lifecycle, Convection, and Radiation during the Cloud, Aerosol and Monsoon Processes Philippines Experiment (CAMP2Ex), Bulletin of the American Meteorological Society, 104, E1179 – E1205, https://doi.org/10.1175/BAMS-D-21-0285.1, 2023.
Rivera, C., Mellqvist, J., Samuelsson, J., Lefer, B., Alvarez, S., and Patel, M. R.: Quantification of NO2 and SO2 emissions from the Houston Ship Channel and Texas City industrial areas during the 2006 Texas Air Quality Study, Journal of Geophysical Research: Atmospheres, 115, https://doi.org/https://doi.org/10.1029/2009JD012675, 2010.
Robins, J.: A new approach to causal inference in mortality studies with a sustained exposure period—application to control of the healthy worker survivor effect, Mathematical Modelling, 7, 1393–1512, https://doi.org/https://doi.org/10.1016/0270-0255(86)90088-6, 1986.
Romps, D. M., Latimer, K., Zhu, Q., Jurkat-Witschas, T., Mahnke, C., Prabhakaran, T., Weigel, R., and Wendisch, M.: Air Pollution Unable to Intensify Storms via Warm-Phase Invigoration, Geophysical Research Letters, 50, e2022GL100 409, https://doi.org/https://doi.org/10.1029/2022GL100409, e2022GL100409 2022GL100409, 2023.
Rosenfeld, D., Lohmann, U., Raga, G. B., O'Dowd, C. D., Kulmala, M., Fuzzi, S., Reissell, A., and Andreae, M. O.: Flood or Drought: How Do Aerosols Affect Precipitation?, Science, 321, 1309–1313, https://doi.org/10.1126/science.1160606, 2008.
Ryzhkov, A. V., Giangrande, S. E., Melnikov, V. M., and Schuur, T. J.: Calibration Issues of Dual-Polarization Radar Measurements, Journal of Atmospheric and Oceanic Technology, 22, 1138 – 1155, https://doi.org/10.1175/JTECH1772.1, 2005.
Sanderson, B., Piani, C., and Ingram, W.: Towards constraining climate sensitivity by linear analysis of feedback patterns in thousands of perturbed-physics GCM simulations, Clim Dyn, 30, 175 – 190, https://doi.org/https://doi.org/10.1007/s00382-007-0280-7, 2008.
Singh, A. and Kuang, C.: Condensation Particle Counter (CPC) Instrument Handbook, DOE/SC-ARM-TR-145, https://doi.org/10.2172/1245983, 2024.
Storer, R. L., Van Den Heever, S. C., and Stephens, G. L.: Modeling aerosol impacts on convective storms in different environments, Journal of the Atmospheric Sciences, 67, 3904–3915, 2010.
Storer, R. L., van den Heever, S. C., and L'Ecuyer, T. S.: Observations of aerosol-induced convective invigoration in the tropical east Atlantic, Journal of Geophysical Research: Atmospheres, 119, 3963–3975, https://doi.org/https://doi.org/10.1002/2013JD020272, 2014.
Sun, M., Qie, X., Mansell, E. R., Liu, D., Yair, Y., Fierro, A. O., Yuan, S., and Lu, J.: Aerosol Impacts on Storm Electrification and Lightning Discharges Under Different Thermodynamic Environments, Journal of Geophysical Research: Atmospheres, 128, e2022JD037 450, https://doi.org/https://doi.org/10.1029/2022JD037450, e2022JD037450 2022JD037450, 2023.
Takahashi, H., Luo, Z. J., Stephens, G., and Mulholland, J. P.: Revisiting the Land-Ocean Contrasts in Deep Convective Cloud Intensity Using Global Satellite Observations, Geophysical Research Letters, 50, e2022GL102 089, https://doi.org/https://doi.org/10.1029/2022GL102089, e2022GL102089 2022GL102089, 2023.
Tan, J., Jakob, C., and Rossow, W.: Increases in tropical rainfall driven by changes in frequency of organized deep convection, Nature, 519, 451–454, https://doi.org/https://doi.org/10.1038/nature14339, 2015.
Tao, W.-K., Lang, S., Zeng, X., Shige, S., and Takayabu, Y.: Relating Convective and Stratiform Rain to Latent Heating, Journal of Climate, 23, 1874 – 1893, https://doi.org/10.1175/2009JCLI3278.1, 2010.
Tao, W.-K., Chen, J.-P., Li, Z., Wang, C., and Zhang, C.: Impact of aerosols on convective clouds and precipitation, Reviews of Geophysics, 50, 2012.
Uin, J., Aiken, A. C., Dubey, M. K., Kuang, C., Pekour, M., Salwen, C., Sedlacek, A. J., Senum, G., Smith, S., Wang, J., Watson, T. B., and Springston, S. R.: Atmospheric Radiation Measurement (ARM) Aerosol Observing Systems (AOS) for Surface-Based In Situ Atmospheric

Aerosol and Trace Gas Measurements, Journal of Atmospheric and Oceanic Technology, 36, 2429 – 2447, https://doi.org/10.1175/JTECH-D-19-0077.1, 2019.

van den Heever, S. C. and Cotton, W. R.: Urban Aerosol Impacts on Downwind Convective Storms, Journal of Applied Meteorology and Climatology, 46, 828 – 850, https://doi.org/10.1175/JAM2492.1, 2007.

van den Heever, S. C., Carrió, G. G., Cotton, W. R., DeMott, P. J., and Prenni, A. J.: Impacts of Nucleating Aerosol on Florida Storms. Part I: Mesoscale Simulations, Journal of the Atmospheric Sciences, 63, 1752 – 1775, https://doi.org/10.1175/JAS3713.1, 2006.

van den Heever, S. C., Fridlind, A. M., Marinescu, P. J., Heiken-feld, M., White, B., and Stier, P.: Aerosol-Cloud-Precipitation-Climate (ACPC) initiative: Deep Convective Cloud Grouproadmap, ACPC Rep., p. 13, http://acpcinitiative.org/Docs/ACPC_DCC_Roadmap_171019.pdf, 2018.

van den Heever, S. C., Grant, L. D., Freeman, S. W., Marinescu, P. J., Barnum, J., Bukowski, J., Casas, E., Drager, A. J., Fuchs, B., Herman, G. R., Hitchcock, S. M., Kennedy, P. C., Nielsen, E. R., Park, J. M., Rasmussen, K., Razin, M. N., Riesenberg, R., Dellaripa, E. R., Slocum, C. J., Toms, B. A., and van den Heever, A.: The Colorado State University Convective CLoud Outflows and UpDrafts Experiment (C3LOUD-Ex), Bulletin of the American Meteorological Society, 102, E1283 – E1305, https://doi.org/10.1175/BAMS-D-19-0013.1, 2021.

Varble, A.: Erroneous attribution of deep convective invigoration to aerosol concentration, Journal of the Atmospheric Sciences, 75, 1351–1368, 2018.

Varble, A. C., Nesbitt, S. W., Salio, P., Hardin, J. C., Bharadwaj, N., Borque, P., DeMott, P. J., Feng, Z., Hill, T. C. J., Marquis, J. N., Matthews, A., Mei, F., Öktem, R., Castro, V., Goldberger, L., Hunzinger, A., Barry, K. R., Kreidenweis, S. M., McFarquhar, G. M., McMurdie, L. A., Pekour, M., Powers, H., Romps, D. M., Saulo, C., Schmid, B., Tomlinson, J. M., van den Heever, S. C., Zelenyuk, A., Zhang, Z., and Zipser, E. J.: Utilizing a Storm-Generating Hotspot to Study Convective Cloud Transitions: The CACTI Experiment, Bulletin of the American Meteorological Society, 102, E1597 – E1620, https://doi.org/10.1175/BAMS-D-20-0030.1, 2021.

Varble, A. C., Igel, A. L., Morrison, H., Grabowski, W. W., and Lebo, Z. J.: Opinion: A critical evaluation of the evidence for aerosol invigoration of deep convection, Atmospheric Chemistry and Physics, 23, 13 791–13 808, 2023.

Veals, P. G., Varble, A. C., Russell, J. O., Hardin, J. C., and Zipser, E. J.: Indications of a decrease in the depth of deep convective cores with increasing aerosol concentration during the cacti campaign, Journal of the Atmospheric Sciences, 79, 705–722, 2022.

Wallace, H. W., Sanchez, N. P., Flynn, J. H., Erickson, M. H., Lefer, B. L., and Griffin, R. J.: Source apportionment of particulate matter and trace gases near a major refinery near the Houston Ship Channel, Atmospheric Environment, 173, 16–29, https://doi.org/https://doi.org/10.1016/j.atmosenv.2017.10.049, 2018.

Wang, D., Giangrande, S., Bartholomew, M. J., Hardin, J. C., Feng, Z., Thalman, R., and Machado, L.: The Green Ocean: Precipitation Insights from the GoAmazon2014/5 experiment, Atmospheric Chemistry and Physics, 18, https://www.osti.gov/biblio/1605429, 2018.

Wang, D., Giangrande, S. E., Schiro, K. A., Jensen, M. P., and Houze Jr, R. A.: The characteristics of tropical and midlatitude mesoscale convective systems as revealed by radar wind profilers, Journal of Geophysical Research: Atmospheres, 124, 4601–4619, 2019.

Wang, D., Giangrande, S. E., Feng, Z., Hardin, J. C., and Prein, A. F.: Updraft and downdraft core size and intensity as revealed by radar wind profilers: MCS observations and idealized model comparisons, Journal of Geophysical Research: Atmospheres, 125, e2019JD031 774, 2020a.

Wang, D., Jensen, M. P., D'Iorio, J. A., Jozef, G., Giangrande, S. E., Johnson, K. L., Luo, Z. J., Starzec, M., and Mullendore, G. L.: An Observational Comparison of Level of Neutral Buoyancy and Level of Maximum Detrainment in Tropical Deep Convective Clouds, Journal of Geophysical Research: Atmospheres, 125, e2020JD032 637, https://doi.org/https://doi.org/10.1029/2020JD032637, e2020JD032637 10.1029/2020JD032637, 2020b.

Wang, D., Jensen, M. P., Taylor, D., Kowalski, G., Hogan, M., Wittemann, B. M., Rakotoarivony, A., Giangrande, S. E., and Park, J. M.: Linking Synoptic Patterns to Cloud Properties and Local Circulations Over Southeastern Texas, Journal of Geophysical Research: Atmospheres, 127, e2021JD035 920, https://doi.org/https://doi.org/10.1029/2021JD035920, e2021JD035920 2021JD035920, 2022a.

Wang, D., Prein, A. F., Giangrande, S. E., Ramos-Valle, A., Ge, M., and Jensen, M. P.: Convective Updraft and Downdraft Characteristics of Continental Mesoscale Convective Systems in the Model Gray Zone, Journal of Geophysical Research: Atmospheres, 127, e2022JD036 746, https://doi.org/https://doi.org/10.1029/2022JD036746, e2022JD036746 2022JD036746, 2022b.

Wang, D., Melvin, E., Smith, N., Jensen, M., Gupta, S., Abdullah-Smoot, A., Pszeniczny, N., and Hahn, T.: TRACER Perspectives on Gulf-Breeze and Bay-Breeze Circulations and Coastal Convection, Monthly Weather Review, 2024.

Weisman, M. L. and Klemp, J. B.: The Structure and Classification of Numerically Simulated Convective Stormsin Directionally Varying Wind Shears, Monthly Weather Review, 112, 2479 – 2498, https://doi.org/10.1175/1520-0493(1984)112<2479:TSACON>2.0.CO;2, 1984.

Welch, B.: The generalization of "Student's" problem when several different population variances are involved, Biometrika, 34, 28–35, https://doi.org/10.1093/biomet/34.1-2.28, 2005.

Wellmann, C., Barrett, A. I., Johnson, J. S., Kunz, M., Vogel, B., Carslaw, K. S., and Hoose, C.: Using Emulators to Understand the Sensitivity of Deep Convective Clouds and Hail to Environmental Conditions, Journal of Advances in Modeling Earth Systems, 10, 3103–3122, https://doi.org/https://doi.org/10.1029/2018MS001465, 2018.

Yoon, S., Ortiz, S. M., Clark, A. E., Barrett, T. E., Usenko, S., Duvall, R. M., Ruiz, L. H., Bean, J. K., Faxon, C. B., Flynn, J. H., Lefer, B. L., Leong, Y. J., Griffin, R. J., and Sheesley, R. J.: Apportioned primary and secondary organic aerosol during pollution events of DISCOVER-AQ Houston, Atmospheric Environment, 244, 117 954, https://doi.org/https://doi.org/10.1016/j.atmosenv.2020.117954, 2021.

Zang, L., Rosenfeld, D., Pan, Z., Mao, F., Zhu, Y., Lu, X., and Gong, W.: Observing Aerosol Primary Convective Invigoration and Its Meteorological Feedback, Geophysical Research Letters, 50, e2023GL104 151, https://doi.org/https://doi.org/10.1029/2023GL104151, e2023GL104151 2023GL104151, 2023.

Zhang, Y., Fan, J., Li, Z., and Rosenfeld, D.: Impacts of cloud microphysics parameterizations on simulated aerosol–cloud interactions for deep convective clouds over Houston, Atmospheric Chemistry and Physics, 21, 2363–2381, https://doi.org/10.5194/acp-21-2363-2021, 2021.

Zipser, E. J. and LeMone, M. A.: Cumulonimbus Vertical Velocity Events in GATE. Part II: Synthesis and Model Core Structure, Journal of Atmospheric Sciences, 37, 2458 – 2469, https://doi.org/10.1175/1520-0469(1980)037<2458:CVVEIG>2.0.CO;2, 1980.

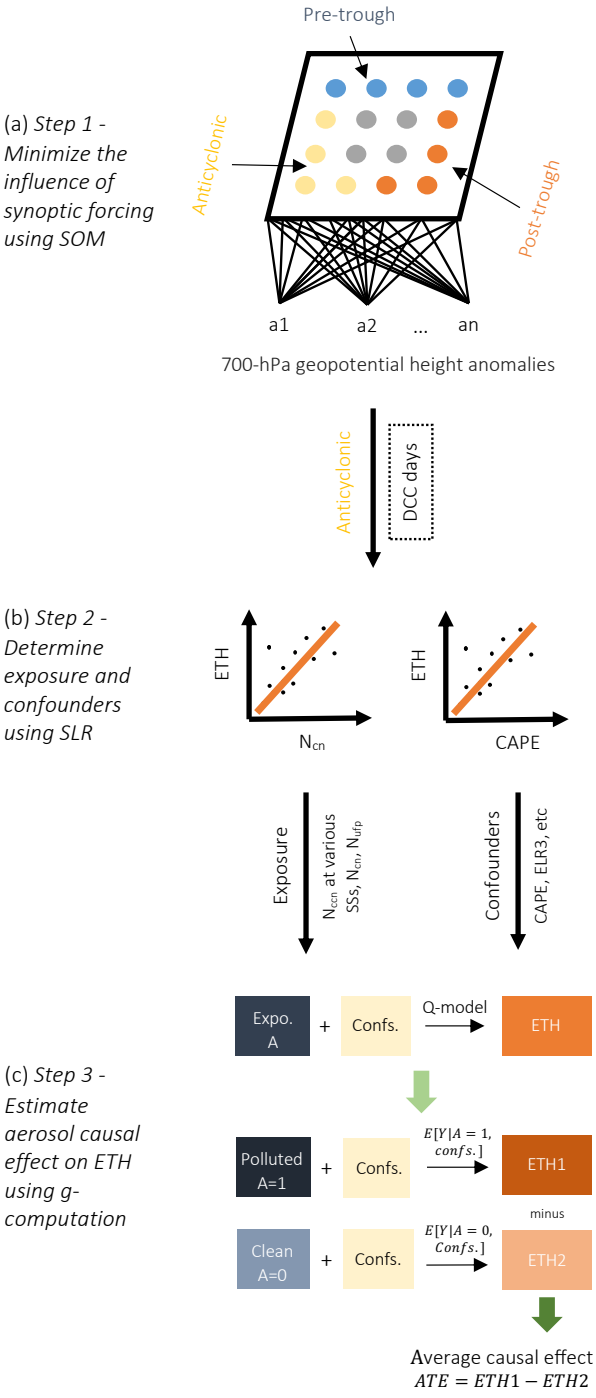

Figure 1. Flow chart of the causal model framework used to estimate the causal effect of aerosols on DCC ETH.

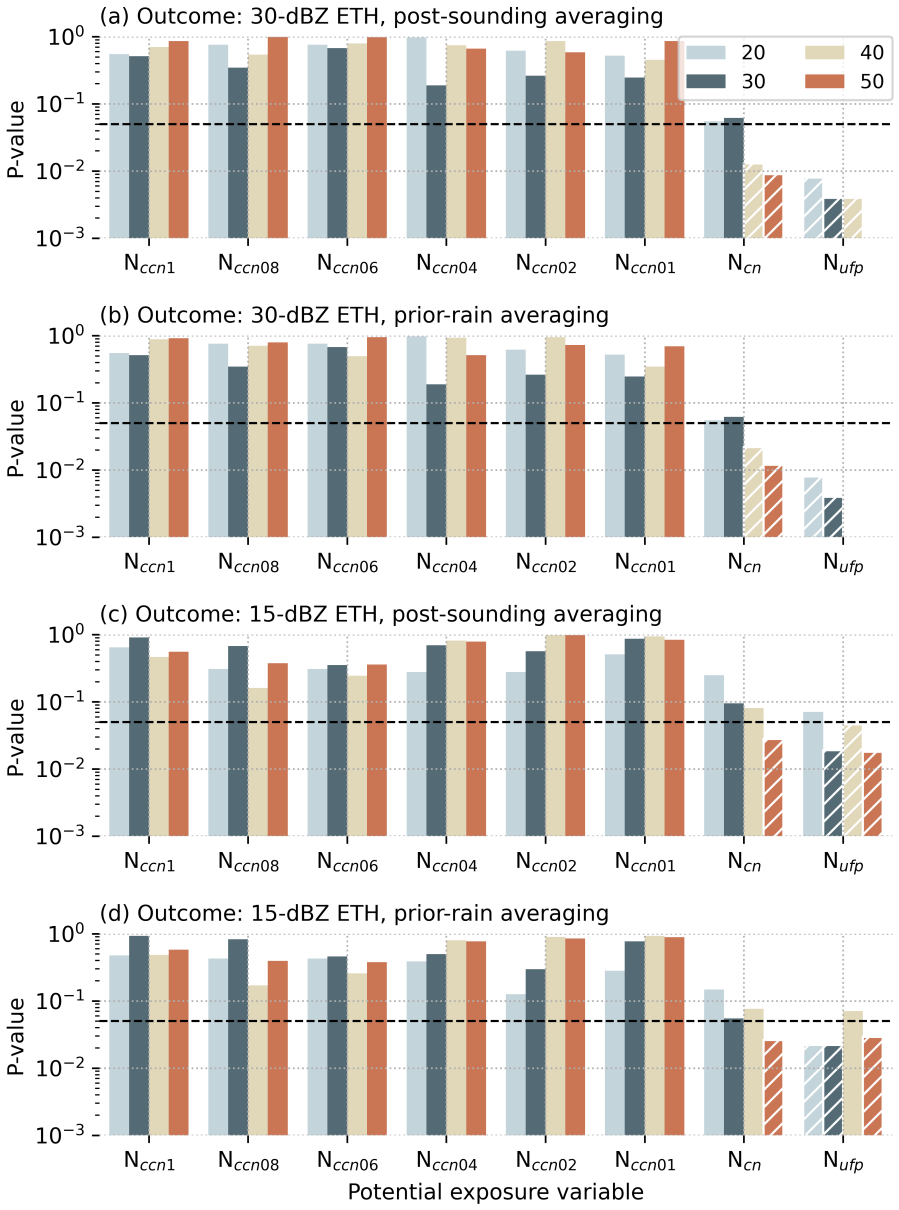

Figure 2. Simple linear regression model *P*-value for each aerosol number concentration as a predictor (potential exposure variable) respectively for different aerosol averaging periods. Different colors represent different maximum distances between aerosol and DCC measurements (km in radius from the M1 site). The horizontal line indicates $P = 0.05$ and the white hatch lines indicate valid models ($P < 0.05$). Note that for some models, the *P*-value is zero which is not visible on the plot.

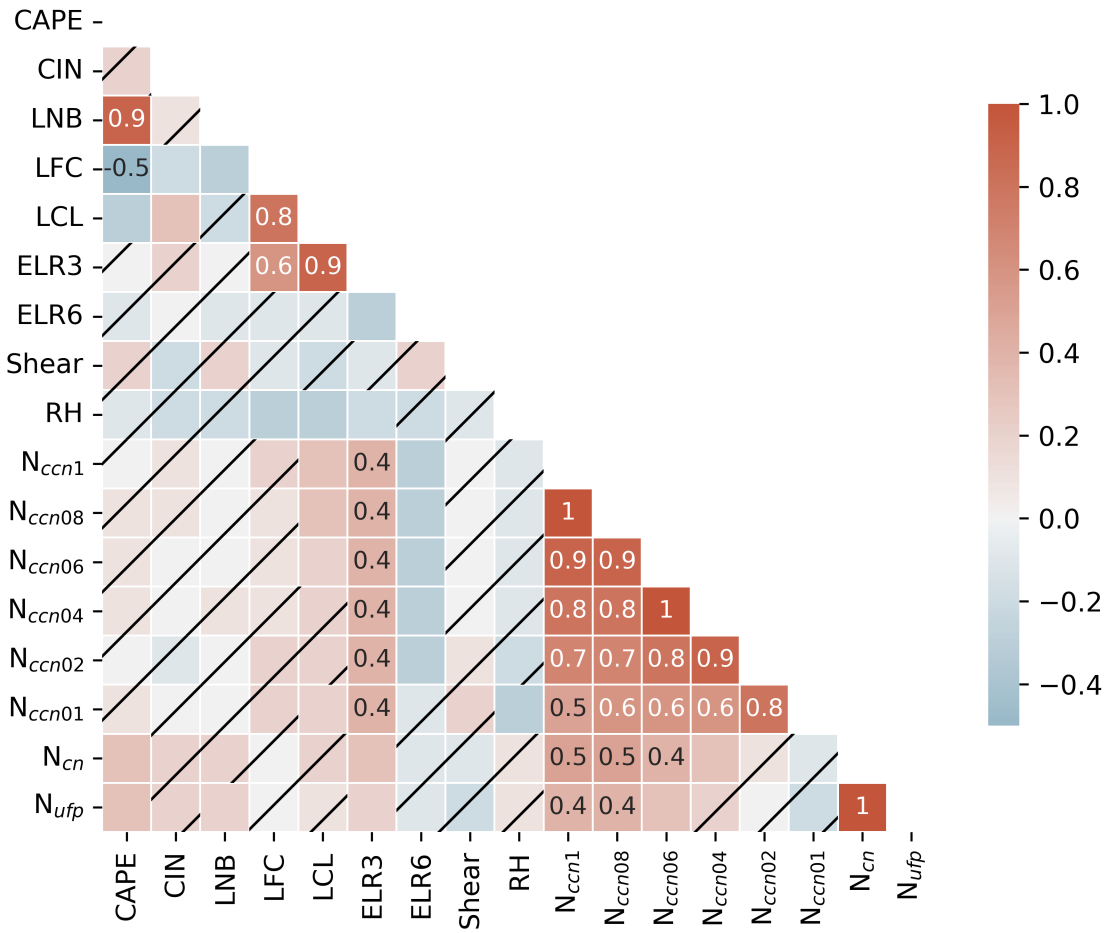

Figure 3. Correlation matrix between the meteorological variables and aerosol number concentrations for DCC cases identified within a radius of 50 km from the M1 site. The correlation matrix is a table showing Pearson *R*-values between sets of variables. The meteorological variables are calculated using ARM soundings when assuming the most-unstable parcel would rise to form a convection. The black hatch lines indicate non-significant *R*-values.

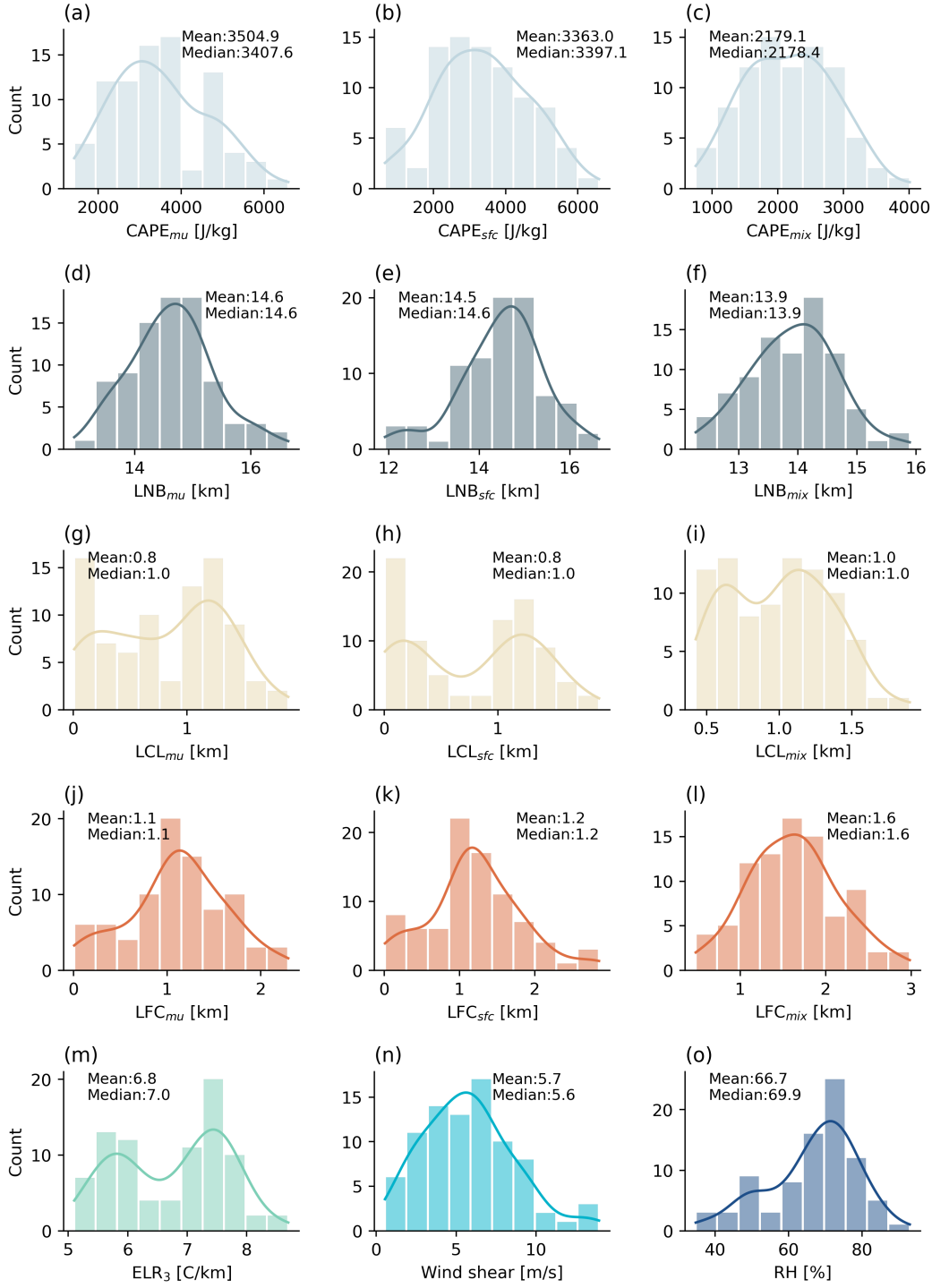

Figure 4. Histograms with density kernel estimation (solid lines) of meteorological variables from the ARM soundings launched prior to DCC cases identified within a radius of 50 km from the M1 site. The bin size is defined by the difference between the maximum and minimum values of each variable divided by the number of bins, which is fixed at 10 for each subplot.

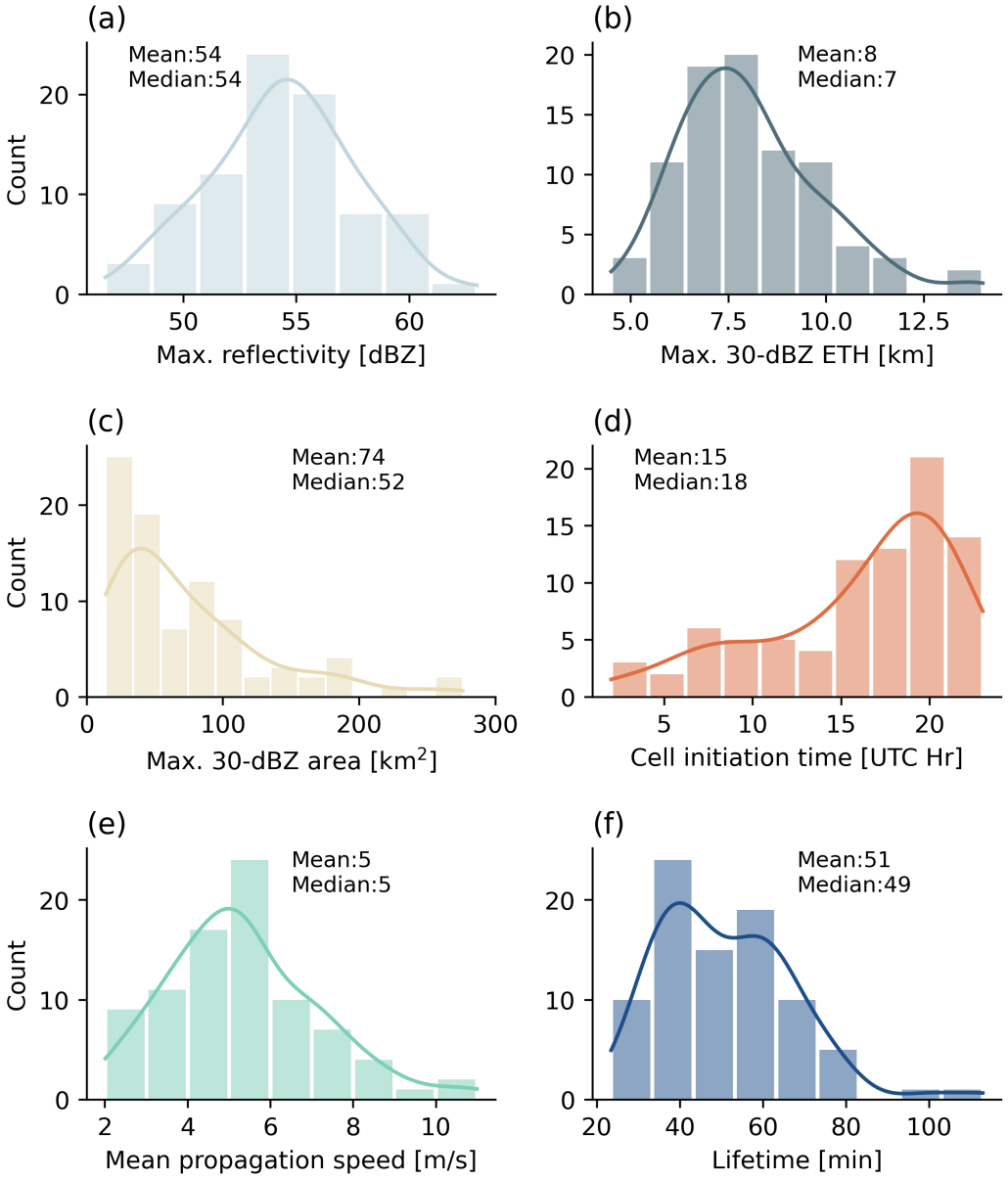

Figure 5. Histograms with density kernel estimation (solid lines) of the maximum 2-km radar reflectivity, 30-dBZ ETH, and 30-dBZ rainfall core area along with initiation time, mean propagation speed, lifetime for each DCC rainfall core identified within a radius of 50 km from the M1 site. The binwidth is set to 2 dBZ for (a), 1 km for (b), 20 km^2 for (c), 2 hrs for (d), 0.5 m/s for (e), and 10 min for (f).

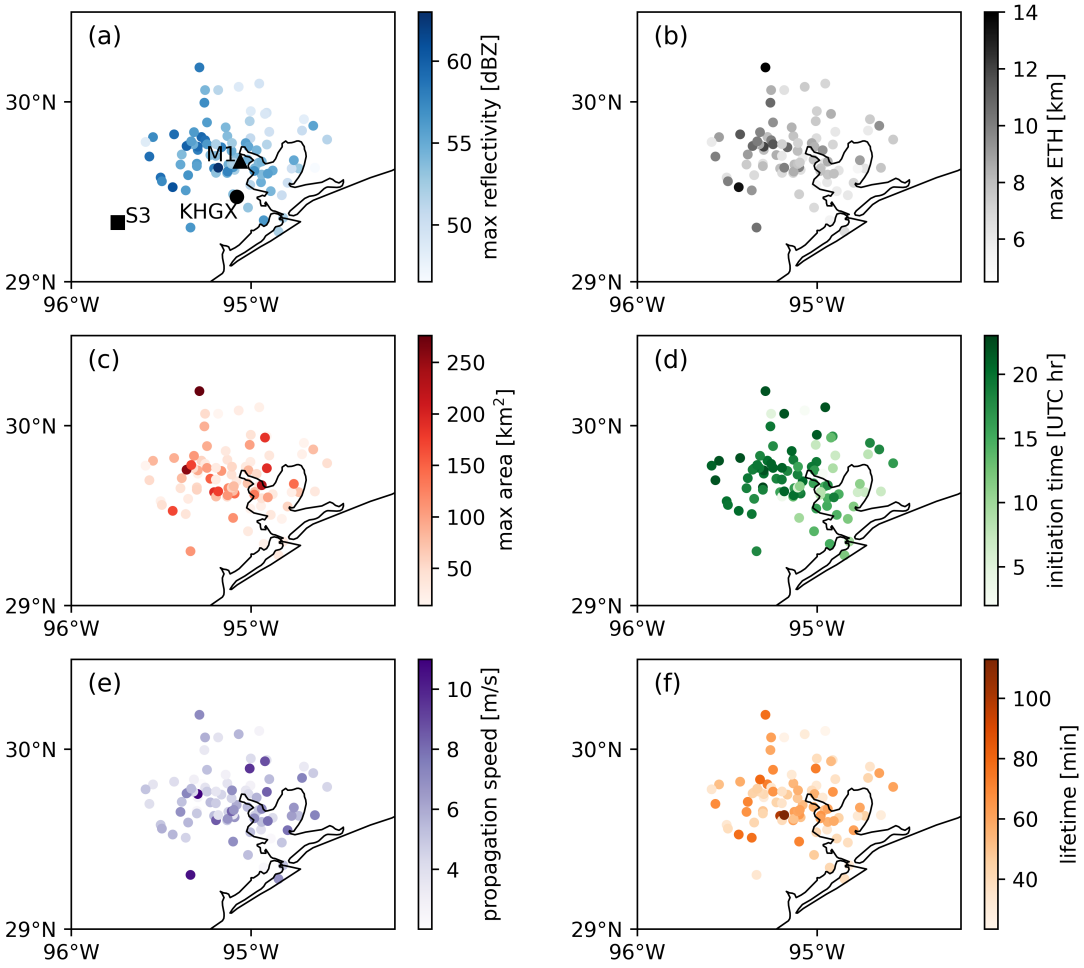

Figure 6. Dots indicate locations where the cell ETHs are maximized on maps for cells initiated within 50 km of the M1 site. The colors in these subplots indicate cell properties as shown in Figure 5.

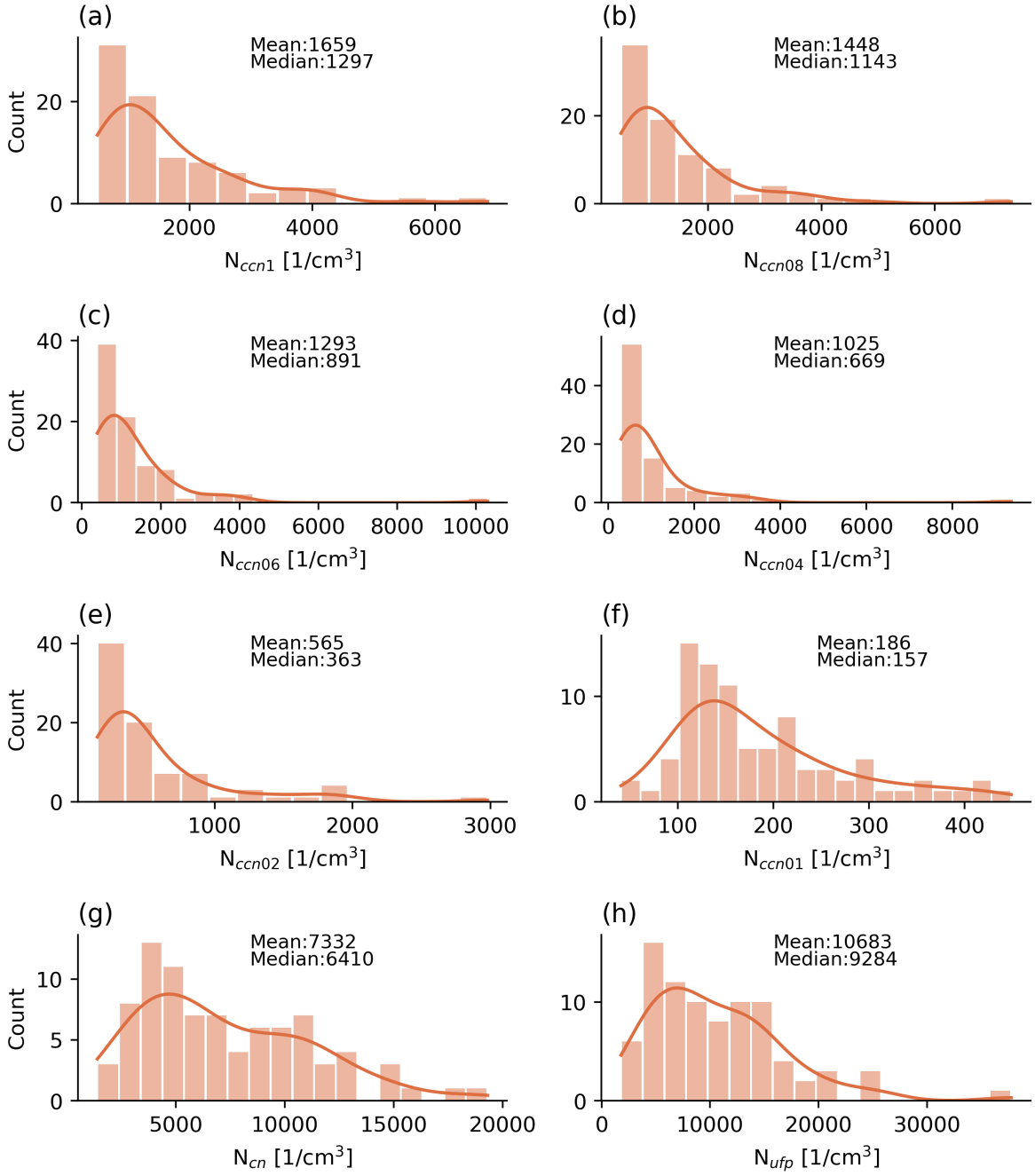

Figure 7. Histograms with density kernel estimation (solid lines) of CCN number concentrations measured at different SS levels and total aerosol number concentrations for DCC cases identified within a radius of 50 km from the M1 site. The binwidth is set to 500 cm^{-3} for (a)-(d), 200 cm^{-3} for (e), 20 cm^{-3} for (f), 1,000 cm^{-3} for (g), and 2,000 cm^{-3} for (h).

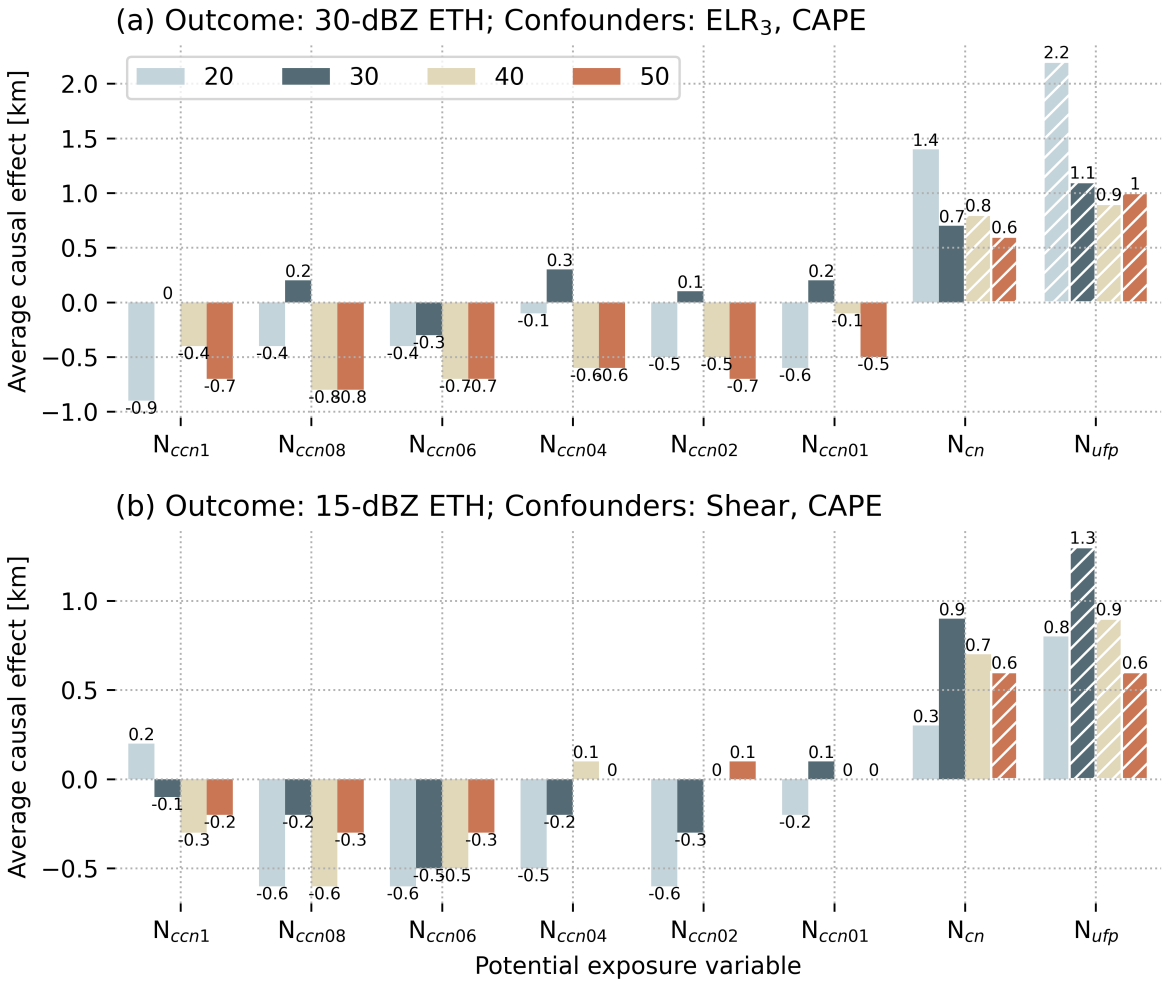

Figure 8. Average causal effects on (a) 30-dBZ ETH and (b) 15-dBZ ETH estimated for each potential exposure variable after controlling for confounders. Different colors represent different maximum distances between measurements of environmental variables and DCC properties. The meteorological variables are calculated using ARM soundings (6-hr) when assuming the most-unstable parcel would rise to form a convection. The white hatch lines indicate valid results.

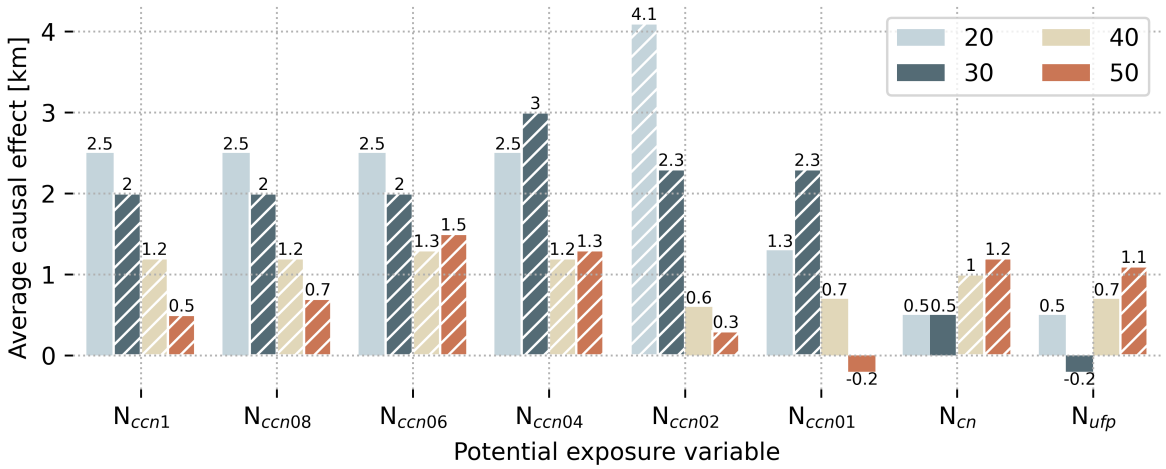

Figure 9. Average causal effects on 30-dBZ ETH estimated for each potential exposure variable after controlling for confounders (ELR_3 and CAPE) for DCCs identified during sea-breeze days only. The post-sounding aerosol averaging period is considered. Different colors represent different maximum distances between measurements of environments and DCCs. The meteorological variables are calculated using ARM soundings (6-hr) when assuming the most-unstable parcel would rise to form a convection. The white hatch lines indicate valid results.

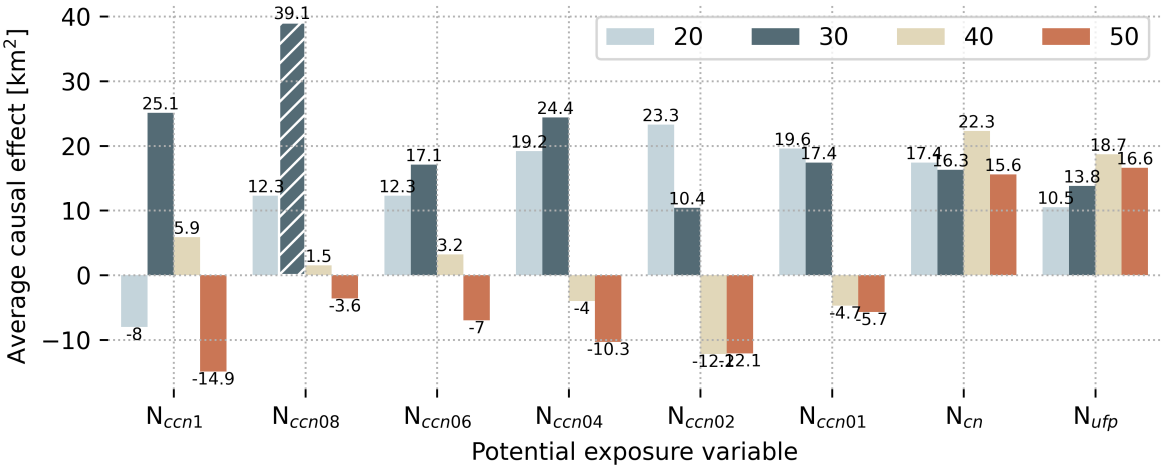

Figure 10. Same as Figure 8a but for cell area as outcome variable and CAPE as confounding variable.

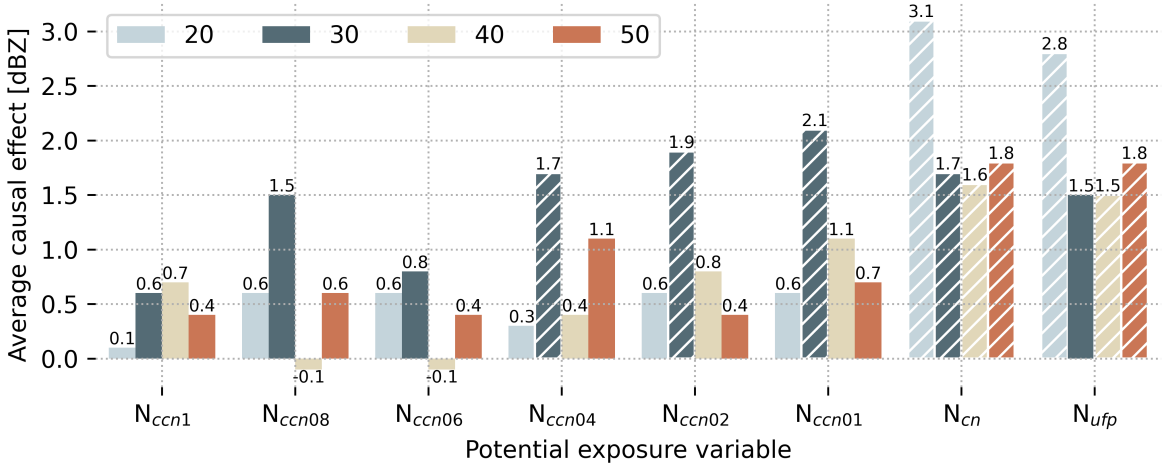

Figure 11. Same as Figure 8a but using maximum reflectivity as outcome variable and CAPE as confounding variable.

Table 1. Explanations of each term in the g-computation model with examples.

Terms	Explanations	Examples
Exposure variable / Independent variable	It is a variable whose causal effect on another variable (outcome) is being investigated. It represents the condition being manipulated or analyzed in hypothetical scenarios.	Aerosol number concentration, CCN number concentration
Outcome variable / Dependent variable	It is the variable of interest for which we aim to estimate the causal effect of an exposure. By applying g-computation, potential outcomes under varying exposure levels can be simulated, allowing for the assessment of differences between exposure scenarios.	Convective cloud 30-dBZ echo top height
Confounder / Confounding variable	They are variables, other than the one being studied (the exposure), that are associated with both the outcome and the exposure. They can distort or mask the true effect of the exposure on the outcome, leading to inaccurate conclusions about the relationship between the two.	Convective Available Potential Energy (CAPE), Environmental Lapse Rate (ELR)

Table 2. Number of DCC cases tracked in 2022 from June to September when considering different radii to the M1 site and under different scenarios.

Distance to M1	6-hr soundings	4-hr soundings	Sea-breeze days, 6-hr soundings
20 km	43	29	12
30 km	61	46	22
40 km	70	54	29
50 km	86	70	38

Table 3. Pearson correlation coefficients (*R*-values) between convective indices and DCC ETH. The most-unstable parcel is used in the calculations of the convective indices. DCCs were identified within different distances, ranging from 20 to 50 km, from the ARM M1 site. Only the *R*-values that pass the significance tests are included.

Distance to M1	LNB	CAPE	LCL	LFC	ELR_3	ELR_6	LWS	RH
Outcome variable: 30-dBZ ETH								
20 km	×	×	×	×	×	×	×	×
30 km	×	×	×	×	0.3	×	×	×
40 km	×	0.3	0.2	×	0.3	×	×	×
50 km	0.2	0.2	0.3	×	0.4	×	×	×
Outcome variable: 15-dBZ ETH								
20 km	×	×	×	×	×	×	-0.3	×
30 km	×	×	×	×	×	×	×	×
40 km	×	×	×	×	×	×	×	×
50 km	0.2	0.3	×	×	×	×	×	×

Table 4. Average causal effects on ETH [km] using different confounders and outcome variables under different scenarios.

Confounders	CAPE_{mu}, ELR_3	CAPE_{sfc}, ELR_3	CAPE_{mix}, ELR_3
6-hr soundings, post-sounding averaging			
30-dBZ ETH	1.0	1.0	1.0
15-dBZ ETH	0.8	0.7	0.8
6-hr soundings, prior-rain averaging			
30-dBZ ETH	1.1	1.1	1.1
15-dBZ ETH	1.4	0.8	0.8
4-hr soundings, post-sounding averaging			
30-dBZ ETH	1.2	1.2	1.2
15-dBZ ETH	1.2	1.2	1.3
4-hr soundings, prior-rain averaging			
30-dBZ ETH	1.2	1.2	1.2
15-dBZ ETH	1.1	1.1	1.2

Supporting Information for

Causal Analysis of Aerosol Impacts on Isolated Deep Convection: Findings from TRACER

Dié Wang[1], Roni W. Kobrosly[2], Tao Zhang[1], Tamanna Subba[1], Susan C. van den Heever[3], Siddhant Gupta[4], Michael P. Jensen[1]

1. Brookhaven National Laboratory, Upton, NY 11937
2. Icahn School of Medicine at Mount Sinai, New York, NY 10029
3. Colorado State University, Fort Collins, CO 80523
4. Argonne National Laboratory, Lemont, IL 60439

Contents of this file

Deleted: 3

Deleted: 9

Text S1. TINT algorithm

Tracking convective rainfall cores initiated during DCC days in the anticyclonic regime is accomplished using the TINT algorithm, developed by Raut et al. (2021). TINT, an open-source tracking tool, automatically estimates the trajectories of moving cloud objects in sequential images, applicable to various two-dimensional datasets, including remote sensing measurements and model simulations (Fridlind et al. 2019). For a detailed explanation of the TINT algorithm, refer to Raut et al. (2021).

The inputs for TINT are derived from the 2-km *Z* values derived from gridded NEXRAD KHGX-Houston radar data (1 km horizontal resolution). The selection of the 2 km level is made to accurately sample precipitation areas, following the method presented in Oue et al. (2022). The position of each cell is determined as the difference-weighted center of the region with *Z* exceeding a certain threshold value. Tracking is conducted for all selected DCC days, starting from 0500 LT and continuing until 0459 LT the following day. To ensure the optimal performance of TINT, several thresholds are applied:

- Definition of contiguous object: To mitigate signal noise contamination, a single object is characterized as a contiguous area including a minimum of eight radar grid points (1 km × 1 km) with a minimum *Z* threshold of 10 dBZ, signifying the presence of precipitation echoes.
- Identification of convective cells: An object is labeled as a convective cell if its highest 2-km *Z* exceeds 30 dBZ. This threshold is widely used by radar systems for detecting convective clouds, as demonstrated in studies such as Petersen et al. (1996), Kumar et al. (2016), and Gupta et al. (2023).
- Definition of deep convective event: A deep convective event is defined as a track with a 2-km *Z* exceeding 40 dBZ and a 30-dBZ echo top height (ETH) higher than 5 km at any point during its lifespan, following a similar definition to Dixon and Wiener (1993). Convective cells during these events are called convective rainfall cores which are used in our study.
- Domain exclusion: Convective rainfall cores that move into or out of the radar domain (400 km × 400 km) during their life cycle are excluded from the statistical analysis.
- Lifetime duration: To minimize potential misidentification due to uncertainties in radar data or the tracking method, the analysis primarily focuses on deep convection with rainfall cores lasting longer than 40 minutes. This criterion ensures that the convective rainfall cores are detected in at least 7 or 8 consecutive radar scans.

Text S2. Definitions of key DCC parameters

Several key parameters are derived and analyzed for these tracked convective rainfall cores, including the maximum 2-km *Z*, rainfall core area, 30-dBZ ETH/15-dBZ ETH, core lifetime, and core propagation speed. Here is a summary of these key parameters:

1. Maximum 2-km *Z*: This parameter represents the highest intensity of radar reflectivity observed within the convective cells. It indicates the strength of the precipitation and provides information about the intensity of the convective activity.
2. Core lifetime: The lifetime of a convective rainfall core is determined by the duration between its first identification time and its last identification time. This parameter provides insights into how long the precipitating cells persist in the study region on average.
3. Core area: The core area is calculated by multiplying the number of continuous grid points with 2-km *Z* greater than 30 dBZ by the grid resolution. It provides an estimate of the spatial extent covered by the convective rainfall cores and indicates the size of the area experiencing moderate precipitation.
4. 30-dBZ ETH/15-dBZ ETH: The ETH is defined as the maximum height at which the radar echo reaches a Z of 30 dBZ/15 dBZ. It serves as a proxy for the strength of the convective updraft or upward mass flux, providing information about the vertical extent and intensity of the convective activity (Heymsfield et al., 2010).
5. Core propagation speed: The propagation speed of a convective rainfall core is determined as the mean rate at which a cell advances from its first radar detected location to its final radar detected position.
6. Initiation timing and location: These parameters indicate when and where the rainfall cores first develop. They provide insights into the preferred timing and spatial distribution of rainfall initiation in the radar region.

It is important to note that the TINT algorithm used in our study is not designed to efficiently identify the splitting and merging of convective cores, which can be more prevalent in organized convective systems. As a result, this limitation may have some impact on the estimation of convective properties in those clouds. However, our study specifically focuses on relatively isolated DCCs, which is a common type of DCC in southeastern Texas during the summer months in the anticyclonic regime (Fridlind et al., 2019). In these isolated cases, the occurrence of mergers and splitters is relatively less frequent compared to organized DCCs. Therefore, we anticipate that the impact of this limitation of TINT on our statistical analysis of convective rainfall core life cycle characteristics will be minimal.

Text S3. Sensitivity tests of tracking thresholds

We conducted sensitivity tests to evaluate the robustness of the criteria used in defining and tracking convective rainfall cores in the prior subsection. The tests were performed using data from June to August 2022 (regardless of SOM regimes), and the results are summarized in Table S3. Here are the details of the sensitivity tests and their impact on DCC properties:

1. Single object definition: In this test, a single object was defined as a contiguous area of at least 10 radar grid points with a minimum 2-km *Z* threshold of 10 dBZ. This resulted in a 5% reduction in the total number of cells, and a slight increase of 5 km^2 in the median core area compared to the original criteria.
2. Tracking using 3-km *Z*: In this test, the tracking of cells was performed using a 3-km *Z* threshold. No significant changes were found in terms of the convective properties of interest.
3. Decreased lifetime threshold: The DCC lifetime limit was decreased from 40 minutes to 30 minutes in this test. As expected, the number of cores significantly increased by 32%, and the median rainfall core lifetime was shortened by 8 minutes.
4. Calibration offset: To account for the possible NEXRAD *Z* offset mentioned in previous studies (Gourley et al., 2003; Ryzhkov et al., 2005), an offset of 3 dBZ was applied to the data. This test aimed to investigate the potential impact of the calibration issue on derived convective properties. The results showed that this calibration offset had only a slight impact on the number of cores and core properties of interest.

Overall, the mean state of core properties was somewhat sensitive to the thresholds used in the tracking model, but most of the changes were insignificant according to results from a *t*-test. The most significant changes in cell core area occurred when the lifetime threshold was loosened. However, no significant differences are found in terms of 30-dBZ ETH when using different thresholds.

Text S4. Key assumptions of the MLR models

We evaluate the MLR models by assessing and validating the key assumptions. These assumptions include linearity, homoscedasticity, normality, independence, and multicollinearity. In the following paragraphs, we provide a detailed analysis and explanation of these tests and plots. Overall, the results indicate that the data meet the essential assumptions of the MLR model. This fulfillment of assumptions strengthens the reliability of the following estimated causal effects of aerosols.

To test for linearity, we examine whether there is a linear relationship between the predictor variable and the outcome variable by plotting the model residuals as a function of the fitted variables. The residuals are the differences between the observed and predicted values of the outcome variable after fitting a linear model to the data. The fitted values, on the other hand, are the predicted values of the outcome variable based on the MLR model. As illustrated in Figure S5, when using DCC cases identified within a radius of 50 km from the M1 site, the residuals are evenly spread around a horizontal line with no distinct patterns when considering different exposures, indicating the absence of non-linear relationships. Similar patterns are shown for other scenarios considered in the study. This provides some evidence for linearity between the outcome and predictor variables in our data.

To validate the assumption of homoscedasticity in the MLR model, we create a Spread-Location or Scale-Location plot as shown in Figure S6. The plot is generated by plotting the square root of the absolute value of the standardized residuals on the y-axis against the fitted values on the x-axis. The standardized residuals were calculated by dividing the residuals by their estimated standard deviation, resulting in a mean of zero and a standard deviation of one. When the assumptions of linearity and constant variance are met, the Spread-Location plot will show a roughly horizontal line with no discernible pattern, indicating that the residuals have a constant variance across the range of fitted values. In Figure S6, the red line is close to being horizontal, and the points are equally and randomly spread, indicating good homoscedasticity. We find similar results for other scenarios considered in the study.

For validating the assumption of normality in the MLR model, we employ a quantile-quantile (QQ) plot of standardized residuals plotted against theoretical quantiles. The theoretical quantiles are the expected values if the data followed a normal distribution. If the standardized residuals are normally distributed, the plot will show a linear relationship between the two sets of values, as depicted in Figure S7. Based on the plot,

we observe that the data closely follows a straight line, indicating that the residuals are normally distributed. Thus, we can conclude that the assumption of normality has been met for our MLR regression model.

Multicollinearity refers to the situation where two or more independent variables in a MLR model are highly correlated with each other. This can lead to unstable regression coefficients, inflated standard errors, and inaccurate predictions. To check for the presence of little or no multicollinearity in this study, we used the Variance Inflation Factor (VIF). The VIF measures the extent to which the variance of the estimated regression coefficient is increased due to multicollinearity. A VIF of 1 indicates no multicollinearity, while a VIF greater than 1 suggests the presence of multicollinearity. Typically, a VIF greater than 5 or 10 is a cause for concern.

When using the most-unstable parcel and the first data pairing method, the VIF values for three covariates in the model for predicting 30-dBZ ETH are all around 1, which suggest limited multicollinearity. Note that standardizing the covariates significantly reduces the VIF value for all predictors, and we, therefore, used the standardized covariates for subsequent calculations of g-computation. When using different parcels as the surface or mixed-layer parcel, the VIF values only change slightly, but are all below 2.

The independence of observations in the MLR model is assessed using the Durbin-Watson test. This test is a statistical method used to test for the presence of autocorrelation in the residuals. Autocorrelation refers to the situation where the residuals are correlated with each other over time, which violates the assumption of independence. The Durbin-Watson test calculates a test statistic that ranges from 0 to 4. A value of 2 indicates that there is no autocorrelation, while a value below 2 indicates positive autocorrelation, and a value above 2 indicates negative autocorrelation. Typically, a value between 1.5 and 2.5 is considered acceptable. The Durbin-Watson values for all scenarios are around 2, which indicates that our observations are independent of each other. Therefore, we can conclude that there is no evidence of autocorrelation in the residuals of our MLR models.

Assessing the influence of individual observations on the results of a regression analysis is crucial in identifying and eliminating any strong influencers. To accomplish this, a leverage plot is conducted to show the leverage values of each case against the standardized residuals. Leverage values represent the degree to which an observational point can affect the slope of the regression line. Observations with high leverage values

and large standardized residuals have the potential to strongly impact the slope, coefficients, or other aspects of the model, such as the statistical significance of the predictors. These observations may be outliers or may have extreme values of the predictor variables, meaning that they do not follow the trend observed in most cases. Cook's distance, which measures the influence of an observation on the regression coefficients, is used in conjunction with the leverage plot to identify influential observations. Typically, a cutoff value of 1 is used, which is plotted as a red dashed line in Figure S8. This means that any observation with a Cook's distance greater than 1 is considered influential. In our dataset, all cases are below the Cook's distance cutoff values, indicating that they have low Cook's distance scores and do not have a large impact on the estimated regression results. Similar results are shown for other scenarios as well.

Table S1. Intense operation days during the TRACER Intense Operation Period in 2022.

Date (MMDD)
0601, 0602, 0604, 0617, 0621, 0622, 0626, 0629, 0706, 0710, 0711, 0712, 0713, 0727, 0729, 0730, 0801, 0802, 0804, 0807, 0808, 0809, 0810, 0821, 0822, 0826, 0827, 0828, 0831, 0901, 0902, 0906, 0907, 0916, 0917, 0918, 0919, 0925

Table S2. Correlation coefficients between meteorological variables and ETH when the surface parcel or mix-layer parcel is used in the calculations of the meteorological variables.

Distance to M1	LNB	CAPE	LCL	LFC	ELR_3	ELR_6	LWS	RH
30-dBZ ETH, Surface Parcel								
20 km	x	x	x	x	x	x	x	x
30 km	x	x	0.3	x	0.3	x	x	x
40 km	x	0.3	0.3	x	0.3	x	x	x
50 km	0.3	0.2	0.4	x	0.4	x	x	x
30-dBZ ETH, Mixed-layer Parcel								
20 km	x	x	x	-0.3	x	x	x	x
30 km	x	x	0.4	x	0.3	x	x	x
40 km	x	x	0.3	x	0.3	x	x	x
50 km	0.2	x	0.4	x	0.4	x	x	x
15-dBZ ETH, Surface Parcel								
20 km	x	x	x	x	x	x	-0.3	x
30 km	x	x	x	x	x	x	x	x
40 km	x	x	x	x	x	x	x	x
50 km	x	x	x	x	x	x	x	x
15-dBZ ETH, Mixed-layer Parcel								
20 km	x	x	x	x	x	x	-0.3	x
30 km	x	x	x	x	x	x	x	x
40 km	x	x	x	x	x	x	x	x
50 km	0.3	0.3	x	x	x	x	x	x

Table S3. DCC properties from several sensitivity tests performed on three-month data from June to August in 2022.

Z threshold [dBZ]	Min. no. of grid	Min. lifetime [min]	Level of Z for tracking [km]	No. of samples	Median max. Z [dBZ]	Median core area [km2]	Median 30-dBZ ETH [km]	Median lifetime [min]
30	8	40	2	9568	46.4	47	6.5	80
30	10	40	2	9149	46.8	52	7	80
30	8	40	3	9689	46.4	47	7	80
30	8	30	2	12635	46.0	42	6.5	72
33	8	40	2	8434	47.5	45	6.5	78

Table S4. The Adjusted R^2 values for the fitted MLR models and the 95% confidence intervals for the independent variables. The outcome variable is the 30 dBZ ETH and the CAPE is calculated when assuming the most unstable parcel would rise.

Exposure, Distance to the ARM site	Adjusted R^2	95% confidence intervals for the exposure variables	95% confidence intervals for CAPE	95% confidence intervals for ELR_3
All cases				
N_{cn}, 40 km	0.2	[-0.01, 1.53]	[0.03, 0.78]	[-0.02, 0.76]
N_{cn}, 50 km	0.2	[-0.07, 1.37]	[-0.02, 0.69]	[0.35, 1.06]
N_{ufp}, 20 km	0.1	[0.66, 3.76]	[-0.67, 0.66]	[-1.16, 0.39]
N_{ufp}, 30 km	0.2	[0.16, 2.02]	[-0.11, 0.76]	[-0.12, 0.81]
N_{ufp}, 40 km	0.2	[0.11, 1.66]	[0.01, 0.75]	[-0.04, 0.73]
N_{ufp}, 50 km	0.3	[0.32, 1.73]	[-0.06, 0.63]	[0.32, 1.01]
Sea breeze cases only				
N_{ccn1}, 30 km	0.2	[-0.01, 4.06]	[-0.63, 1.18]	[-0.65, 1.32]
N_{ccn1}, 40 km	0.2	[-0.43, 2.73]	[-0.44, 1.02]	[-0.32, 1.10]
N_{ccn1}, 50 km	0.3	[-0.68, 1.61]	[-0.00, 1.06]	[0.29, 1.42]
N_{ccn08}, 30 km	0.2	[-0.01, 4.06]	[-0.63, 1.18]	[-0.65, 1.32]
N_{ccn08}, 40 km	0.2	[-0.57, 3.01]	[-0.47, 1.04]	[-0.51, 1.08]
N_{ccn08}, 50 km	0.3	[-0.70, 2.05]	[-0.14, 1.01]	[0.14, 1.40]
N_{ccn06}, 30 km	0.2	[-0.01, 4.06]	[-0.63, 1.18]	[-0.65, 1.32]
N_{ccn06}, 40 km	0.2	[-0.29, 2.95]	[-0.33, 1.04]	[-0.52, 1.02]
N_{ccn06}, 50 km	0.4	[0.29, 2.66]	[-0.15, 0.87]	[0.01, 1.15]
N_{ccn04}, 30 km	0.3	[0.74, 5.30]	[-0.63, 1.05]	[-1.32, 0.90]
N_{ccn04}, 40 km	0.2	[-0.57, 3.01]	[-0.47, 1.04]	[-0.51, 1.08]
N_{ccn04}, 50 km	0.4	[0.06, 2.62]	[-0.23, 0.87]	[0.02, 1.20]
N_{ccn02}, 20 km	0.4	[0.75, 7.44]	[-1.07, 1.20]	[-2.76, 0.75]

N_{ccn02}, 30 km	0.3	[0.37, 4.27]	[-0.32, 1.36]	[-0.79, 1.17]
N_{ccn02}, 50 km	0.3	[-0.84, 1.54]	[-0.02, 1.06]	[0.29, 1.46]
N_{ccn01}, 30 km	0.3	[0.37, 4.27]	[-0.32, 1.36]	[-0.79, 1.17]
N_{cn}, 40 km	0.2	[-0.41, 2.41]	[-0.17, 1.15]	[-0.30, 1.11]
N_{cn}, 50 km	0.4	[0.22, 2.26]	[-0.12, 0.89]	[0.41, 1.38]
N_{ufp}, 50 km	0.4	[0.05, 2.16]	[-0.10, 0.93]	[0.33, 1.35]

Formatted: Indent: First line: 0"

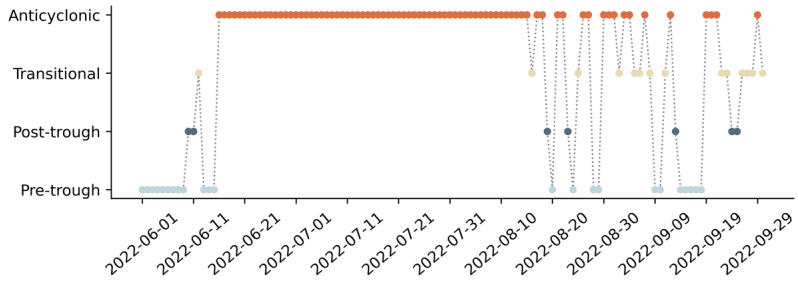

Figure S1. Synoptic regimes as a function of day for 2022, classified using the Self-Organizing Map.

Deleted:

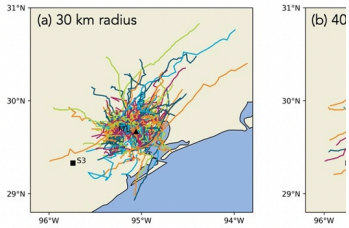

Deleted:
Figure S1. Maps of locations of precipitation core formation and cell tracks identified for¶
cells initiated within a radius of 30 km (a), 40 km (b), 50 km (c) from the M1 site using the¶
first data pairing method.¶

Deleted: 2

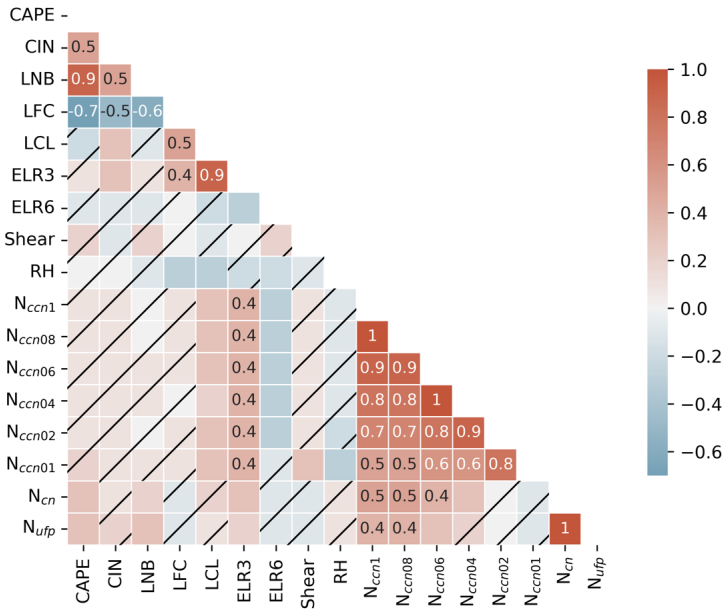

Figure S2. Correlation matrix between the meteorological variables and aerosol number concentrations for DCC cases identified within a radius of 50 km from the M1 site. The meteorological variables are calculated using ARM soundings when assuming the surface parcel would rise to form a convection.

Deleted: 3

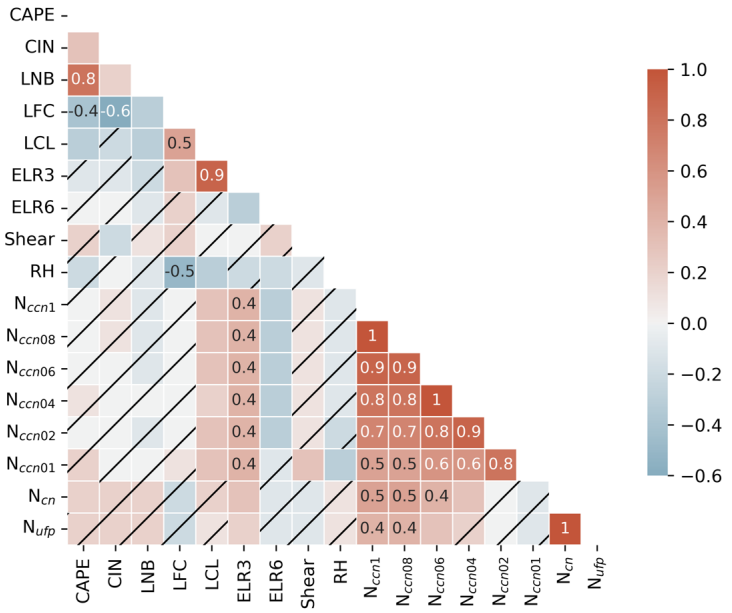

Figure S3. Same as Figure S3 but using a mixed-layer parcel.

Deleted: 4

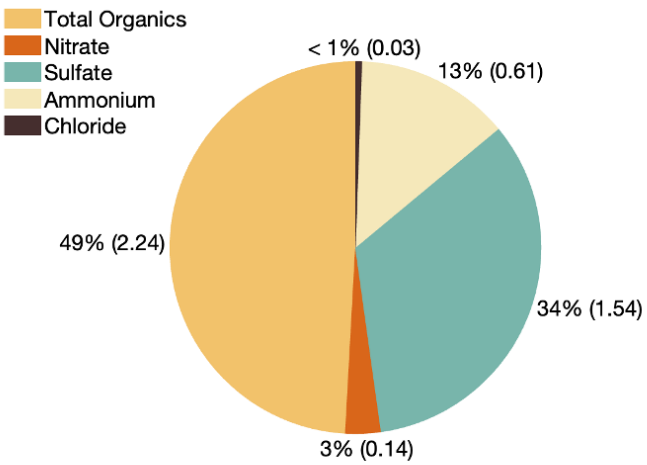

Figure S4. Averaged percentage contribution of aerosol mass concentrations measured during a one-hour period following sounding launches on selected DCC days.

Deleted: 5

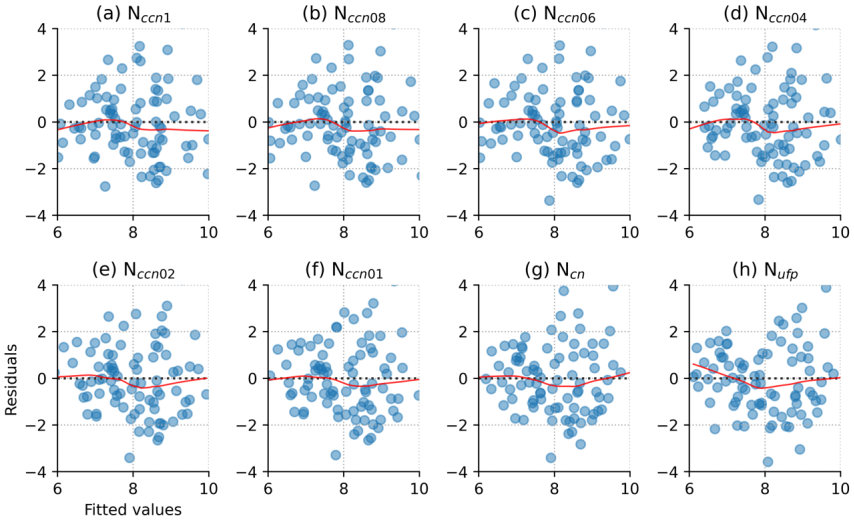

Figure S5. MLR model residuals as a function of fitted values for DCCs formed within a radius of 50 km from the M1 site using the post-sounding data averaging method. The most unstable parcel is used for the calculations of meteorological variables. The outcome variable is 30-dBZ ETH.

Deleted: 6

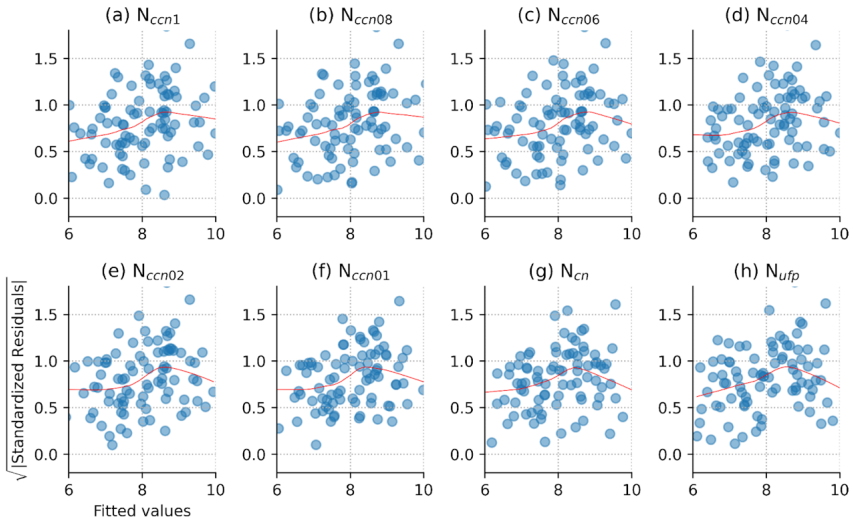

Figure S6. Standardized residuals as a function of fitted values for DCCs formed within a radius of 50 km from the M1 site using the post-sounding data averaging method. The most unstable parcel is used for the calculations of meteorological variables. The outcome variable is 30-dBZ ETH.

Deleted: 7

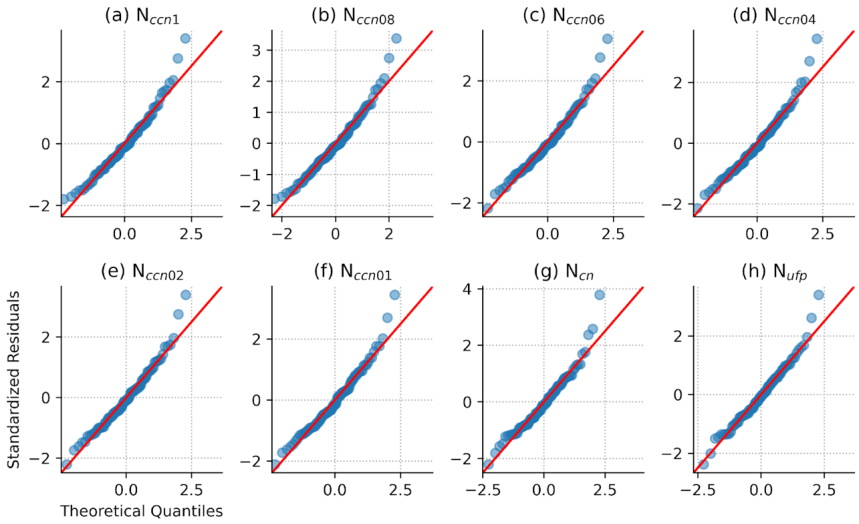

Figure S7. Quantile-quantile plot for DCCs formed within a radius of 50 km from the M1 site using the post-sounding data averaging method. The most unstable parcel is used for the calculations of meteorological variables. The outcome variable is 30-dBZ ETH.

Deleted: 8

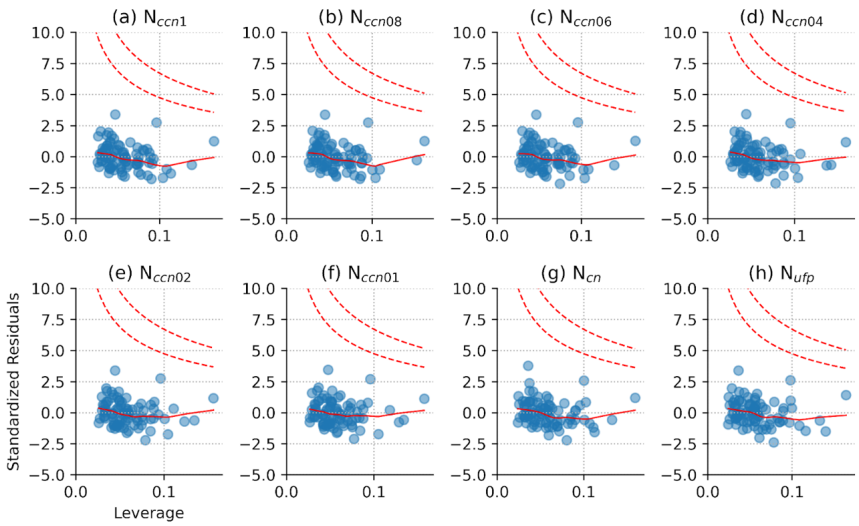

Figure S8. leverage plot for DCCs initiated within a radius of 50 km from the M1 site using the post-sounding data averaging method. The most unstable parcel is used for the calculations of meteorological variables. The outcome variable is 30-dBZ ETH.

Deleted: 9